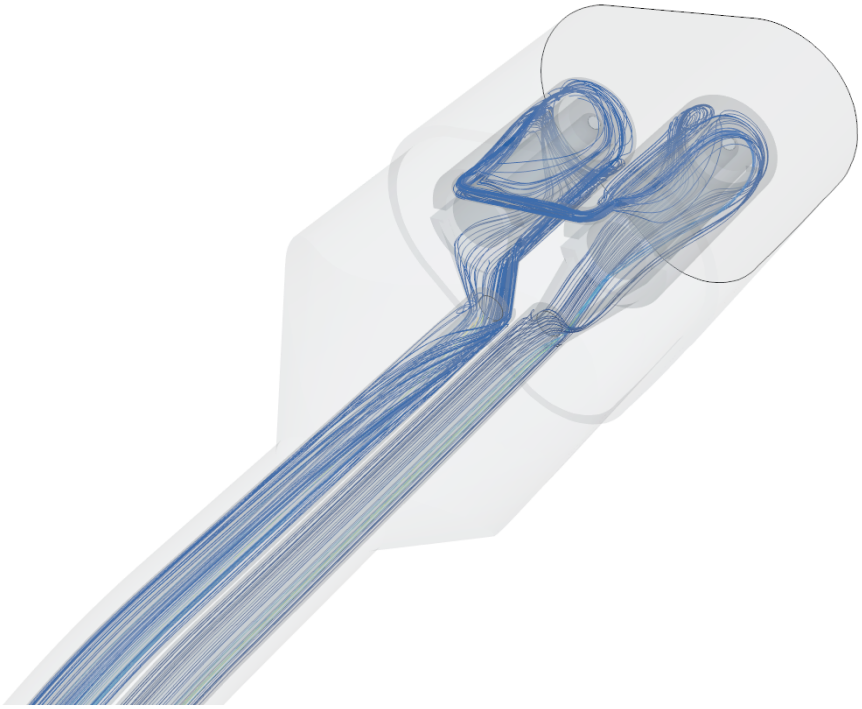

Thermal Management of Electric Vehicle Rapid Charging

Master's thesis in Sustainable Energy Systems

AMIRHOSSEIN BARANI

DEPARTMENT OF MECHANICS AND MARITIME SCIENCES

CHALMERS UNIVERSITY OF TECHNOLOGY
Gothenburg, Sweden 2024
www.chalmers.se

Master's thesis 2024

Thermal Management of Electric Vehicle Rapid Charging

AMIRHOSSEIN BARANI

CHALMERS
UNIVERSITY OF TECHNOLOGY

Department of Mechanics and Maritime Sciences
Division of Vehicle Engineering and Autonomous Systems
Chalmers University of Technology
Gothenburg, Sweden 2024

Thermal Management of Electric Vehicle Rapid Charging
AMIRHOSSEIN BARANI

Supervisor:
Tim Jahnen, Knightec AB
Alexey Vdovin, Chalmers Department of Mechanics and Maritime Sciences

Examiner:
Alexey Vdovin, Chalmers Department of Mechanics and Maritime Sciences

Master's Thesis 2024
Department of Mechanics and Maritime Sciences
Division of Vehicle Engineering and Autonomous Systems
Chalmers University of Technology
SE-412 96 Gothenburg
Telephone +46 31 772 1000

Cover: Streamline visualization constructed in Star CCM+ showing the coolant flow around MCS connector pins.

Typeset in LaTeX
Printed by Chalmers Reproservice
Gothenburg, Sweden 2024

Thermal Management of Electric Vehicle Rapid Charging
AMIRHOSSEIN BARANI
Department of Mechanics and Maritime Sciences
Chalmers University of Technology

Abstract

One of the main barriers to rapid charging of electric vehicles is the thermal management of batteries and charging equipment. Current charging patterns are designed to maintain battery health and safety while avoiding thermal events. Additionally, protection systems monitor the temperature of charging components and, if it exceeds safe limits, reduce power intake to mitigate risks. This increases charging time and impacts the reliability of rapid charging systems. An efficient thermal management system plays a key role in increasing charging stability and enabling faster charging at higher capacities.

This study investigates the thermal management of charging cables and power modules in a Megawatt Charging System (MCS) suitable for heavy-duty vehicles. The research is divided into two parts. First, 3D CFD simulations are conducted for three liquid-cooled cable structures to compare their performance and determine their energy loss and cooling demand. Based on these results, in the second part, four cooling systems (heatsink, heatsink+PCM, liquid cooling, and immersion cooling) are designed for the power modules, and their performance is studied through 1D simulations. The findings provide a holistic view of the capabilities of various thermal management strategies and determine their efficiency in various scenarios.

Considering the oil-cooled charging cable model and the liquid cooling system as the reference, the results demonstrate that charging a heavy-duty EV with a 1 MW MCS under a constant current-constant voltage (CC-CV) charging method for 45 minutes transfers 370 kWh of energy to the battery. The total system efficiency, including power modules and cables, is 97.3%. Of the input energy, 9.12 kWh (2.4%) is lost in the power modules, 0.41 kWh (0.1%) in the charging cable and its cooling system, and 0.34 kWh (0.1%) in the power module cooling system.

Keywords: Megawatt Charging System (MCS), Electric Vehicle Fast Charging, Thermal Management, Liquid-Cooled Cable, Power Module Cooling, EV, BEV, Heavy Duty, Trucks, Rapid Charging, Charging.

Acknowledgements

I would like to express my deepest gratitude to Chalmers University of Technology and Knightec AB for providing me with the opportunity to work on this topic. Their support and resources have been invaluable to the success of this research.

I am especially grateful to Alexey Vdovin and Tim Jahnen for their unwavering support and guidance throughout this project. Their insights and encouragement have greatly contributed to the development and completion of this thesis.

Finally, I acknowledge the use of OpenAI's language model, ChatGPT, for its assistance with grammar checking and enhancing the clarity of this report.

Amirhossein Barani, Gothenburg, June 2024

List of Acronyms

Below is the list of acronyms that have been used throughout this thesis listed in alphabetical order:

AC	Alternating Current
BMS	Battery Management System
CC	Constant Current
CV	Constant Voltage
CFD	Computational Fluid Dynamics
CP	Constant Power
DC	Direct Current
EV	Electric Vehicle
EVSE	Electric Vehicle Supply Equipment
ICEV	Internal Combustion Engine Vehicle
IGBT	Insulated Gate Bipolar Transistor
MCS	Megawatt Charging System
MOSFET	Metal-Oxide-Semiconductor Field-Effect Transistor
OC	Oil-cooled
OD	Outside Diameter
PCB	Printed Circuit Boards
PCM	Phase Change Material
PFC	Power Factor Correction
PM	Power Module
PP	Polypropylene
RANS	Reynolds Averaged Navier-Stokes
RMS	Root Mean Square
SATP	Standard Ambient Temperature and Pressure
SOC	State of Charge
SOH	State of Health
TMS	Thermal Management System
TPU	Thermoplastic polyurethane
WC	Water-cooled
XLPO	Cross Linked Polyolefin

Nomenclature

Below is the list of symbols and terms that have been used throughout this thesis.

A	Area [m^2]
L	Length [m]
r	Radius [m]
t	Time [s]
T	Temperature [K]
V	Voltage [V]
I	Electric Current [A]
μ	Dynamic Viscosity [$Pa \cdot s$]
ν_T	Kinematic Eddy Viscosity
ν	Kinematic Viscosity [m^2/s]
ρ	Density [kg/m^3]
c_p	Specific Heat Capacity [$J/(kg \cdot K)$]
α	Thermal Diffusivity [m^2/s]
h	Heat Transfer Coefficient [$W/(m^2 \cdot K)$]
k	Thermal Conductivity [$W/(m \cdot K)$]; Turbulence Kinetic Energy [J]
Nu	Nusselt Number
P	Pressure [Pa]
Pr	Prandtl Number
q	Heat Transfer [W]
q''	Heat Flux [W/m^2]
Q	Heat energy transferred [J]
$\dot{Q}$	Heat transfer rate [W]
$\dot{m}$	Mass Flow [kg/s]
R	Thermal Resistance [K/W]
Re	Reynolds Number
u, v, w	Velocity in x, y, z directions [m/s]

Contents

List of Figures

List of Tables

1
Introduction

1.1 Background

The global shift towards sustainability has driven the transportation sector to accelerate electrification in order to reduce greenhouse gas emissions. While lightweight electric vehicles (EVs) have rapidly developed, with technology and infrastructure improving year by year, the electrification of heavy-duty vehicles—such as trucks, buses, and commercial fleets—remains a complex challenge. These vehicles require substantially larger batteries and shorter downtime, necessitating high-power charging systems to meet their energy requirements efficiently.

To address this challenge, the Charging Interface Initiative (CharIN), a consortium that includes major global stakeholders in EV manufacturing such as Tesla, ABB, Siemens, and Daimler, has developed the Megawatt Charging System (MCS) standard. MCS is designed specifically for the rapid charging of heavy-duty vehicles, enabling charging at power levels up to 3.75 megawatts (MW). This capability is crucial for minimizing downtime in commercial fleets and ensuring that electric heavy-duty vehicles can meet the demands of industries reliant on long-haul transport and intensive vehicle use.

The implementation of high-power charging systems introduces substantial challenges, particularly in thermal management. The intense heat generated during rapid charging can lead to inefficiencies, component degradation, and safety risks if not properly managed. Effective thermal management is, therefore, crucial to ensuring the reliability, safety, and efficiency of MCS.

This thesis investigates various thermal management strategies for MCS, with a particular focus on cooling techniques for power modules and charging cables. These components are essential in managing the high electrical currents and power levels in megawatt charging.

1.2 Megawatt charging system

The Megawatt Charging System (MCS) is a new standard in EV charging technology, tailored to the demanding requirements of heavy-duty vehicles like trucks and buses. By enabling fast and reliable charging, MCS supports the wider adoption of electric heavy-duty vehicles, contributing to reduced greenhouse gas emissions and more sustainable transportation.

Key technical specifications of the MCS include:

- **Peak Power:** 3.75 MW.
- **Voltage Range:** 500 to 1250 VDC.
- **Maximum Current:** 3000 A DC.

The primary objective of MCS is to facilitate the rapid charging of heavy-duty vehicles, reducing downtime and ensuring continuous operation with minimal interruptions. MCS is designed to charge electric vehicles within 45 minutes, providing sufficient power for up to 4 hours of operation. This rapid charging capability is essential for maintaining the efficiency and productivity of heavy-duty fleets, minimizing the need for extended charging breaks.
The MCS employs a triangular connector, (Figure 1.1). This connector ensures secure and efficient power transfer from the charging station to the vehicle, capable of handling the high power and current levels involved in megawatt charging [1].

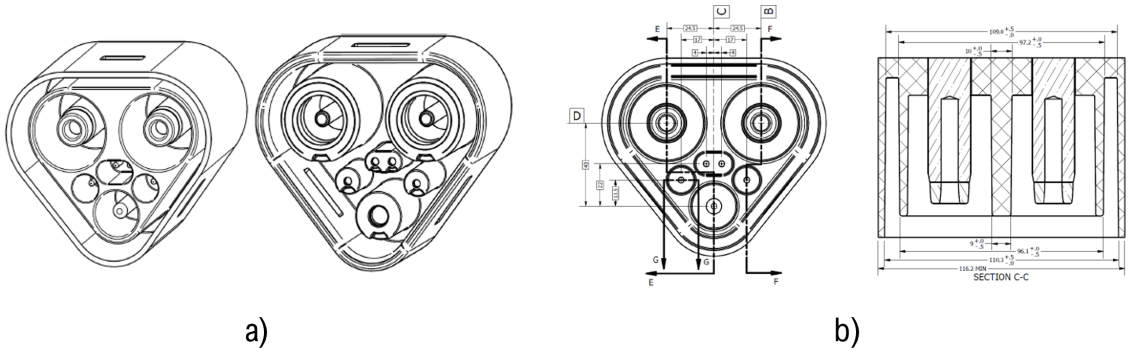

Figure 1.1: MCS connector and socket [1]: (a) layout, (b) dimensions.

1.3 Importance of thermal management in MCS

Effective thermal management is a critical challenge in rapid charging systems, especially in the context of MCS. The high currents required for rapid charging generate significant heat, which can lead to two major issues: potential damage to internal cable components and increased surface temperatures of the cable and connector, posing safety risks. To address these challenges, MCS utilizes liquid-cooled cables, which help maintain safe operating temperatures while allowing the cables to remain lightweight and flexible. Table 1.1 shows the CharIN recommended temperature limits for various MCS cable assembly parts, specifying maximum permissible temperatures for both graspable and touchable components.
In addition to the cables, power modules (PMs) within the MCS are another focal point for thermal management. These modules convert AC current to the appropriate DC output using power electronics such as IGBTs or MOSFETs. These components are significant heat sources, with power losses of approximately 5 to 10 percent, which causes substantial heat generation. Effective thermal management of these components is essential to maintain the equipment's health and efficiency.

Part Type	Maximum Permissible Temperature
Non-metal Parts (Graspable)	60 °C
Non-metal Parts (Touchable)	85 °C
Metal Parts (Graspable)	50 °C
Metal Parts (Touchable)	60 °C
Socket Pins	100 °C

Table 1.1: CharIN recommended temperature limits for MCS cable assembly parts.

In summary, an efficient thermal management system is vital for the stability and performance of Megawatt Charging Systems. It enables faster and safer charging, while also ensuring the longevity and reliability of the equipment involved. By integrating advanced cooling technologies and carefully managing heat dissipation, MCS can achieve the high charging capacities required for heavy-duty electric vehicles.

1.4 Aim and objectives

The primary aim of this research is to investigate various thermal management strategies for MCS, with a particular focus on cooling techniques for power modules and charging cables. This study concentrates on exploring different cooling system options for power modules and evaluating the effectiveness of various charging cable structures, assessing their respective advantages and disadvantages.
Key objectives of the research include:

- **Analysis of thermal management options:** Exploration and assessment of different cooling systems for power modules, including heatsink, heatsink combined with phase change materials (PCM), liquid cooling, and immersion cooling.
- **Evaluation of charging cable structures:** Examination of various designs of charging cables, focusing on their thermal performance.
- **Determination of energy loss:** Quantification of the total energy loss in the MCS and identification of the contribution of each component to the overall energy loss.
- **Comparison of efficiency:** Comparison of the efficiency of different thermal management strategies and cable designs, highlighting their pros and cons in terms of performance, reliability, and practicality.

By achieving these objectives, the research aims to provide valuable insights into optimizing the thermal management of MCS. This will improve charging stability, efficiency, and safety for heavy-duty electric vehicles, supporting the adoption of sustainable transportation.

2

Theory

This chapter discusses the essential physics relevant to this research. It begins with fundamental concepts in heat transfer and fluid dynamics, then explores ohmic loss and electrical contact loss.

2.1 Heat transfer

Studying heat transfer is essential in the thermal management of EV chargers. Heat transfer is defined as the transfer of thermal energy due to a spatial temperature difference, governed by the second law of thermodynamics. Heat transfer is classified into three types of conduction, convection, and radiation [2]. Since heat transfer by radiation is negligible at low-temperature differences, this study focuses on heat transfer by conduction and convection which will be explained in the following sections.

2.1.1 Conduction

Conduction is defined as the transfer of energy from more energetic particles to less energetic particles due to interactions between them. Higher temperatures are associated with higher molecular energies. In the presence of a temperature gradient, energy transfer by conduction occurs in the direction of decreasing temperature. Heat transfer by conduction is quantified by a rate equation known as Fourier's law. For a one-dimensional plane, the rate equation is expressed as [2]:

$$q''_{conduction,x} = -k\frac{dT}{dx} \tag{2.1}$$

where $q''_x(\mathrm{W/m^2})$ is the heat flux in one dimension, $k(\mathrm{W/m.K})$ is the thermal conductivity and is a material characteristic, $T(\mathrm{K})$ is the temperature, and $x(\mathrm{m})$ is the distance. Expanding equation 2.1, heat flux in three dimensions is expressed as:

$$\mathbf{q}'' = -k\nabla T = -k\left(\mathbf{i}\frac{dT}{dx} + \mathbf{j}\frac{dT}{dy} + \mathbf{k}\frac{dT}{dz}\right) \tag{2.2}$$

Equation 2.2 shows heat flux in each dimension occurs in the direction opposite to the temperature gradient. It means heat transfers from regions with higher temperatures to lower ones.

2.1.2 Convection

Convection involves heat transfer through fluid movement. It includes energy transfer by random molecular motion (diffusion) and by the bulk (macroscopic) motion of the fluid. Newton's law of cooling describes convective heat transfer:

$$q''_{\text{convection}} = h(T_s - T_\infty) \tag{2.3}$$

Based on this equation, the convective heat flux q''_x (W/m^2) is proportional to the temperature difference between the surface and the fluid, T_s and T_∞, respectively. Here, and h ($\text{W/m}^2 \cdot \text{K}$) is the convective heat transfer coefficient [2].

2.1.3 Thermal resistance

Based on equations 2.1 and 2.3, which define conduction and convection heat flux respectively, thermal resistance is defined as a measure that shows the resistance of a medium in transferring heat. Thermal resistance against conduction is defined as

$$R_{\text{cond,x}} = \frac{\Delta T}{q''_{cond,x}} = \frac{L}{kA} \tag{2.4}$$

where $R_{\text{cond,x}}$ (K/W) is the conduction resistance and L (m) is the thickness of the material, k ($\text{W/m} \cdot \text{K}$) is the thermal conductivity, and A (m^2) is the cross-sectional area. Thermal resistance against convection is defined as

$$R_{\text{conv}} = \frac{\Delta T}{q''_{\text{conv}}} = \frac{1}{hA} \tag{2.5}$$

where R_{conv} (K/W) is the convection resistance and A (m^2) is the cross-sectional area. It can be concluded that the thermal resistance of a medium depends on the geometry and the thermal properties of the medium[3].

2.2 Fluid dynamics

Fluid dynamics is a branch of fluid mechanics that studies the movement of liquids and gases. In this study, fluid dynamics is employed to evaluate the performance of various liquid-cooled cables in an EV rapid charging system. The outcomes of this study include cooling demand and the amount of heat dissipated to the coolant and the ambient during charging. In this study, these analyses are conducted using computational fluid dynamics (CFD).

Computational fluid dynamics (CFD) is a set of techniques to analyze systems involving fluid flow, heat transfer, and associated phenomena such as chemical reactions by means of computer-based simulation. CFD simulations stand on some fundamental equations, including the Continuity Equation, the Momentum Equation (Navier-Stokes Equations), and the Energy Equation. Additionally, a turbulence modeling approach, specifically the Reynolds-Averaged Navier-Stokes (RANS) method, is employed to simulate the flow and simplify the Navier-Stokes equations.

For control volume integration, the finite volume method is utilized, ensuring the precise conservation of properties in each cell. The equations and the turbulence modeling approach used in this study are defined in the following sections[4].

2.2.1 Continuity equation

In CFD, the continuity equation ensures mass conservation in a fluid. It states that the change in mass within a control volume equals the net mass flow into or out of the volume. For unsteady, three-dimensional compressible and incompressible flows, the continuity equation is [4]:

$$\frac{\partial \rho}{\partial t} + \nabla \cdot (\rho \mathbf{u}) = 0 \tag{2.6}$$

where ρ is the fluid density and $\mathbf{u}$ represents the velocity vector components u, v, and w in the x, y, and z directions, respectively. For incompressible flow, where fluid density remains constant, the equation simplifies:

$$\nabla \cdot \mathbf{u} = 0 \tag{2.7}$$

2.2.2 Momentum equation

The momentum equation in CFD, derived from Newton's second law, is crucial for analyzing fluid motion. It states that the change in momentum of a fluid particle equals the sum of forces acting on it. For unsteady, three-dimensional compressible flows, the momentum equations are:

$$\frac{\partial (\rho u)}{\partial t} + \nabla \cdot (\rho u \mathbf{u}) = -\frac{\partial P}{\partial x} + \nabla \cdot (\mu \nabla u) + S_x \tag{2.8}$$

$$\frac{\partial (\rho v)}{\partial t} + \nabla \cdot (\rho v \mathbf{u}) = -\frac{\partial P}{\partial y} + \nabla \cdot (\mu \nabla v) + S_y \tag{2.9}$$

$$\frac{\partial (\rho w)}{\partial t} + \nabla \cdot (\rho w \mathbf{u}) = -\frac{\partial P}{\partial z} + \nabla \cdot (\mu \nabla w) + S_z \tag{2.10}$$

Here, P is the pressure, μ is the dynamic viscosity, and S_x, S_y, and S_z represent source terms such as gravitational or centrifugal forces[5].

2.2.3 Energy equation

The energy equation in CFD describes the transfer and conversion of thermal energy in a fluid, derived from the First Law of Thermodynamics. It accounts for conduction, convection, and radiation, as well as energy sources like chemical reactions and work done on the fluid. The equation is:

$$\frac{\partial (\rho E)}{\partial t} + \nabla \cdot (\rho E \mathbf{u}) = -\nabla \cdot \mathbf{q} + \Phi + S_E \tag{2.11}$$

where E is the internal energy, $\mathbf{q}$ is the heat flux, Φ represents viscous dissipation, and S_E includes energy sources or sinks [4].

2.2.4 Turbulence

Turbulence in CFD refers to the chaotic and irregular behavior of fluid flow, characterized by rapid fluctuations in velocity, pressure, and other properties. This complexity arises from nonlinear interactions between fluid particles, forming vortices and eddies of varying sizes. Key features of turbulence include:

- **Irregularity**: Turbulent flows are chaotic and consist of a wide range of motion scales, from large eddies to small ones.
- **Diffusivity**: Turbulence greatly enhances the mixing and transport of energy, momentum, and species in all three dimensions.
- **Instability**: Turbulence arises at high Reynolds numbers, where convective forces overcome viscous damping, leading to instability and randomness.
- **Three-dimensionality**: Turbulence is inherently three-dimensional, involving vortex stretching and tilting.
- **Energy Dissipation**: Energy in turbulent flows cascades from large to small scales, where it is eventually dissipated as heat, causing turbulence to decay unless continuously energized [5].

Various turbulence models predict fluid behavior in CFD simulations. This research uses the realizable k-epsilon model, which incorporates a realizability constraint on the stress tensor and a revised epsilon equation accounting for energy dissipation. The model equations are [5]:

$$\frac{\partial(\rho k)}{\partial t} + \nabla \cdot (\rho k \mathbf{u}) = \frac{\partial}{\partial x_j}\left(\frac{\mu_t}{\sigma_k}\frac{\partial k}{\partial x_j}\right) + G_k + G_b - \rho\epsilon - Y_M + S_k \tag{2.12}$$

$$\frac{\partial(\rho \epsilon)}{\partial t} + \nabla \cdot (\rho \epsilon \mathbf{u}) = \frac{\partial}{\partial x_j}\left(\frac{\mu_t}{\sigma_\epsilon}\frac{\partial \epsilon}{\partial x_j}\right) + C_1\frac{\epsilon}{k}(G_k + C_3 G_b) - C_2\rho\frac{\epsilon^2}{k + \sqrt{\nu\epsilon}} + S_\epsilon \tag{2.13}$$

In these equations, ρ is the fluid density, k is the turbulence kinetic energy, and ϵ is the turbulence dissipation rate. The term $\mathbf{u}$ represents the fluid velocity, while μ_t is the turbulent viscosity. σ_k and σ_ϵ are the turbulent Prandtl numbers for k and ϵ, influencing how these quantities diffuse through the fluid.
The terms G_k and G_b represent the generation of turbulence kinetic energy from velocity gradients and buoyancy, respectively. Y_M accounts for effects of compressibility, and S_k and S_ϵ are additional terms that can be adjusted for specific needs. The constants C_1, C_2, and C_3 help balance the equations to reflect the turbulence behavior accurately.
This model defines how turbulence is modeled to predict the fluid behavior in the simulations.

2.3 Electrical loss

Electrical loss is the main source of heat in EV charging systems. In this study, electrical loss in the charging cable is calculated to be used as the source of heat in

the simulations. The two main sources of heat in the charging cable are ohmic loss in the DC cables and electrical contact loss at the EV inlet. The theories related to these two sources are discussed in the following sections.

2.3.1 Ohmic loss

Ohmic loss or Joule heating occurs in conductors due to the electrical current. When an electric current passes through a conductor, electrical energy converts into heat. The power loss of this phenomenon is:

$$P_{\text{ohmic}} = I^2 R \tag{2.14}$$

where I is the current through the conductor and R is the resistance [6]. The resistance R of a conductor is a characteristic of the material and is related to its geometry and temperature.

$$R = \frac{\rho L}{A} \tag{2.15}$$

Equation 2.15 gives the resistance (Ω) for a conductor. In this equation L (m) is the length of the conductor, A (m^2) is the cross-sectional area, and ρ is the resistivity of the material which is a function of temperature and is given as:

$$\rho(T) = \rho_0 \left[1 + \alpha(T - T_0)\right] \tag{2.16}$$

where:

- ρ_0 is the resistivity at a reference temperature T_0 ($\Omega \cdot$ m),
- α is the temperature coefficient of resistivity ($^\circ C^{-1}$),
- T is the temperature of the conductor ($^\circ$C),
- T_0 is the reference temperature ($^\circ$C) [6].

For copper, the resistivity ρ_0 at $T_0 = 0^\circ$C is approximately 1.68×10^{-8} $\Omega \cdot$ m, and the temperature coefficient α is approximately 3.93×10^{-3} $^\circ C^{-1}$. Therefore, the resistance as a function of temperature for copper is given by:

$$R(T) = \frac{1.68 \times 10^{-8} \left(1 + 3.93 \times 10^{-3} \times T\right) L}{A} \tag{2.17}$$

Ohmic loss increases significantly in high-current applications like EV rapid charging systems and needs to be managed to ensure efficiency and safety.

2.3.2 Electrical contact loss

Due to the imperfection of contact points, the electrical pathways at the connections are narrower than in other parts of the conductor, causing increased electrical resistance at these points, which leads to electrical loss, Figure 2.1. Considering this source of heat is crucial when studying the thermal management of high-current connection points, such as EV charging inlets. Contact resistance R_c (Ω) under an elastic deformation can be expressed as:

$$R_c = 29 \cdot \frac{\rho_1 + \rho_2}{\sqrt[3]{P \cdot r \left(\frac{1}{E_1} + \frac{1}{E_2}\right)}} \tag{2.18}$$

In this equation, the terms ρ_1 and ρ_2 are the resistivities of the materials ($\Omega.cm$). P is the applied force in grams, r is the contact radius (mm), and E_1 and E_2 are the moduli of elasticity(kg/mm^2) [7].

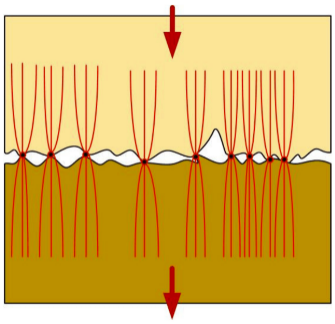

Figure 2.1: Electrical pathways at connection points.

3

Methods

This chapter outlines the methodology used to study the thermal management of an electric vehicle (EV) rapid charging system, focusing on its charging cable and power modules. The proposed charging system utilizes Megawatt Charging System (MCS) technology. It is designed to charge a heavy-duty vehicle with a 600 kWh battery capacity from 20% to 80% state of charge (SOC) in 45 minutes. The voltage range at the EV inlet is 500-1000 VDC, with a maximum current of 1000 amperes and a peak power intake of 1 MW. In this study, the charging system is first designed based on commercially available equipment, and then simulated and analyzed using simulation tools.

3.1 Tools and software

In this study, the following software are used to design, simulate, and analyze the charging system:

- **NX:** NX is a Computer-Aided Design (CAD) software used for 3D design and modeling of the charging cables and connectors required for CFD simulations.
- **COMSOL Multiphysics:** This software is a finite element simulation package suitable for coupled phenomena and multiphysics. COMSOL Multiphysics is used to analyze the thermal and electrical interactions within the connection points at the vehicle inlet; the results are used as the heat source for CFD simulations.
- **StarCCM+:** This tool is used for CFD simulations of the charging cable to model heat dissipation and transfer under various cooling and charging scenarios. The inputs for this software are 3D models from NX. The result of the simulations are used as the inputs for system level simulations.
- **MATLAB Simulink:** MATLAB Simulink, along with the Simscape library, is used for system-level simulation. This environment facilitated the creation of dynamic models to simulate heat transfer in physical systems. Various 1D simulations are conducted to study the system, including the power modules and charging cable, under different cooling strategies.

3.2 Design of the charging system components

3.2.1 Cable and connector design

Based on CharIN's proposal for the MCS charger and connector [8], a model is created for the charging plug and charging Inlet, (Figure 3.1). In the connector model, a coolant pathway is considered around DC connector pins to cool the connection points during charging. The coolant enters the connector from the DC+ side, circulates around the DC+ pin, then moves to the DC- side, circulates around the DC- pin, and finally exits the connector from the DC- side, (Figure 3.2).

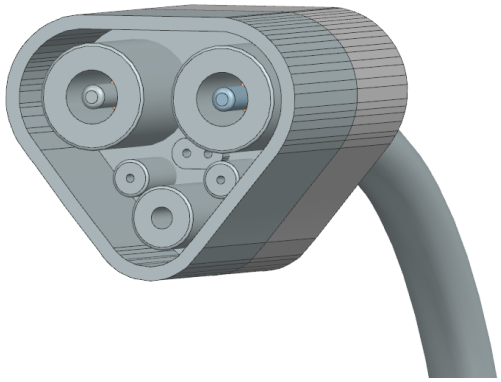

Figure 3.1: MCS connector model.

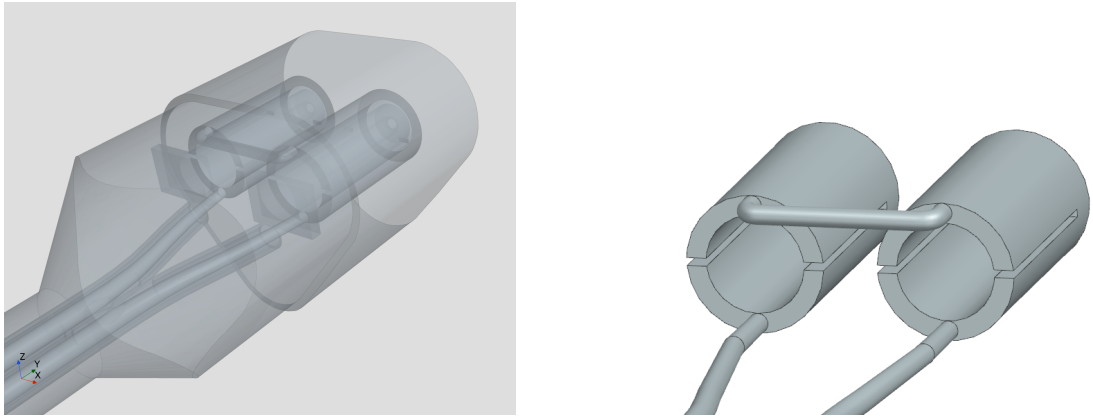

Figure 3.2: Coolant loop around the pins: (a) coolant loop in the connector, (b) coolant loop pass way.

Three different charging cable structures, based on products from **OMG**[1], are considered for this study. chosen structures are detailed in Figures 3.3 and 3.4, showing the different cooling methods and cable configurations. The first two designs use separate channels for the coolant and can be used with both dielectric and non-dielectric

[1] *OMG EV CABLE*, a company based in China specializing in EV charging cables.

materials like water. The third design is intended for cooling with a dielectric cooling medium, where the conductor and coolant are in contact with each other.

Figure 3.3: Water-cooled cable structures: (a) type one (copper-clad water integration), (b) type two (separate cooling channel design)[9].

Construction	Features
Conductor: Bare or tinned copper wire	Rated temperature: -40°C – 90°C
Insulation: XLPO	Rated Voltage: 1500V DC
Filler: PP rope, thermally conductive	Max operating current: 700A
Tape: XLPO	Min Bending Radius: 6×OD
Sheath: TPU	

Table 3.1: Product specifications for water-cooled cables (type one and two)[9].

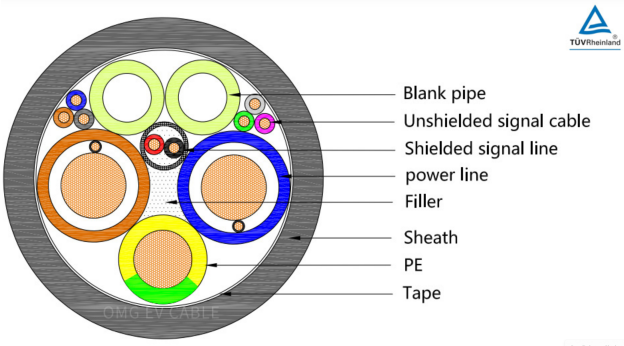

Figure 3.4: Cable structure type three (oil-cooled cable)[9].

Construction	Features
Conductor: Bare Copper	Rated temperature: -40°C – 90°C
Insulation: EVI-1	Rated Voltage: 1500V DC
Filler: PP hemp or cotton yarn	Max operating current: 600A
Tape: Non-woven fabric	Min Bending Radius: 6×OD
Sheath: TPU	

Table 3.2: Product specifications for cable type three[9].

Based on OMG's product datasheets [9], the chosen liquid-cooled cables have a rated voltage of 1500 VDC, with a maximum operating current of 700 A for the water-cooled cable and 600 A for the oil-cooled cable. The nominal capacity of these cables does not match the requirements of this study. The maximum allowable voltage in the desired MCS system is 1000 VDC, which is within the cables' voltage limit, but their maximum current capacity does not meet the 1000 A required for this study. Therefore, the cables need to be scaled up to meet the desired current limit.

The main components in a charging cable include the protective earth wire, communication and connection detection wires, filler materials, insulation materials, DC conductors, and water pipes. Among these elements, the size of the protective earth wire is standardized (25 mm^2) as referenced in [1] and does not need to be scaled up for different capacities. The communication and connection detection wires, as well as the filler materials, are not related to the capacity of the cable and also do not need to be scaled up. The insulation materials prevent the electric current from connecting with other components or escaping the cable. The thickness of the insulation layer depends on the voltage, and since the voltage limit meets the requirements, there is no need to scale up the insulation thickness. On the other hand, the DC conductors are responsible for carrying the current, and their size depends on the current. Therefore, to meet the requirements, the DC conductors need to be scaled up. To accommodate the target system, which requires 1000 volts DC and 1000 amps, the dimensions of the cables were adjusted accordingly.

The current-carrying capacity of a cable is directly related to its cross-sectional area, which depends on the cable's diameter. The cross-sectional area A of a cable with diameter d is given by:

$$A = \pi \left(\frac{d}{2}\right)^2 \tag{3.1}$$

The current-carrying capacity I is proportional to A. Therefore, the relationship between two diameters d_1 and d_2 for currents I_1 and I_2 is:

$$\frac{d_2}{d_1} = \sqrt{\frac{I_2}{I_1}} \tag{3.2}$$

Based on Equation 3.2, the coefficients used to adjust the sizes of the water-cooled and oil-cooled cable conductors are provided in Equations 3.3 and 3.4, respectively.

$$d_{2,WC} = \sqrt{\frac{1000}{700}} \times d_{1,WC} \approx 1.19 \times d_{1,WC} \tag{3.3}$$

$$d_{2,OC} = \sqrt{\frac{1000}{600}} \times d_{1,OC} \approx 1.29 \times d_{1,OC} \tag{3.4}$$

In order to make the models suitable for CFD simulations and reduce the computational cost, elements that do not play a major role in heat generation and dissipation, such as the protective earth wire, communication wires, and connection detection wires, are removed from the models. As shown in Table 3.3, the materials used for

insulation, filler, and sheath have relatively similar material properties. Therefore, as a simplification, a representative material is used for the conductor insulation, coolant insulation, filler, and cable sheath. The properties of this representative material are provided in Table 3.3.

Table 3.3: Material Properties for Insulation Region [2]

Material	Density (kg/m^3)	Specific Heat (J/kg.K)	Thermal Conductivity (W/m.K)
XLPO (Insulation)	920 - 960	2000 - 2250	0.24 - 0.29
PP Rope (Filler)	900 - 920	1900 - 2050	0.22 - 0.25
TPU (Sheath)	1100 - 1250	1800 - 1950	0.20 - 0.25
Model Material	970	2200	0.25

Based on the modification coefficients, simplified models suitable for CFD analysis were created. In these models, Figures 3.5 and 3.6 illustrate cross-sectional views of the liquid-cooled cable models. To streamline these models for CFD simulations, only the components with significant contributions to heat generation and dissipation were considered, while elements with less impact on heat dissipation were treated as insulation material. In these figures, the red color represents the DC+ conductors, blue represents the DC- conductors, cyan represents the coolant, and gray represents the insulation.

Figure 3.5: Water-cooled cable models: (a) Type One (copper-clad water integration), (b) Type Two (separate cooling channel design).

All models were integrated with the MCS connector and inlet. To reflect real-world usage conditions, it is assumed that the cables are 2 meters long, connected to the power dispenser and EV inlet at a height of 0.5 meters, and laid freely on the ground, (Figure 3.7).

[2]Values are provided at SATP conditions (25°C and 1 atm).

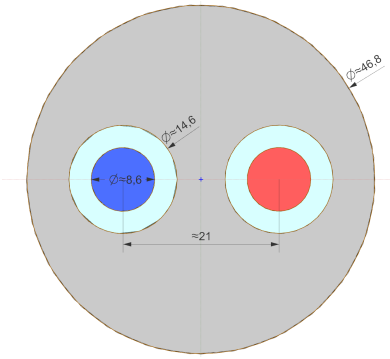

Figure 3.6: Oil-cooled cable model (Type Three).

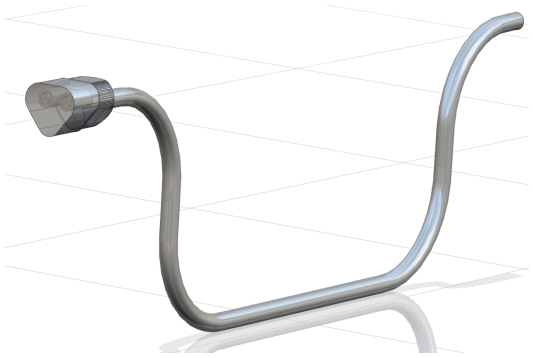

Figure 3.7: Final cable and connector model.

3.2.2 Power module design

For the charger design, the power modules of the HYC400, a charger manufactured by **Alpitronic**[2], were utilized as a reference (Figure 3.8). The HYC400 has an output current of up to 1200 A per charging system and a peak efficiency of 97.5% (Figure 3.9). It features 100 kW power stacks that can be configured with 50 kW granularity, allowing for precise power allocation based on user demand. The output voltage range is from 150 V to 1000 V, with operational temperatures ranging from -30°C to +55°C. The nominal input voltage is 380 V / 400 V / 480 V (rms), with a maximum continuous input current of 600 A (rms) at a frequency of 50 Hz / 60 Hz. Power factor correction is greater than 0.99 due to active PFC, and each power module weighs 115 kg (see Appendix A). In this study, a hypothetical 1 MW EV charger design is conceptualized by using 10 of these 100 kW power modules in parallel.

Figure 3.8: HYC400 EV charger.

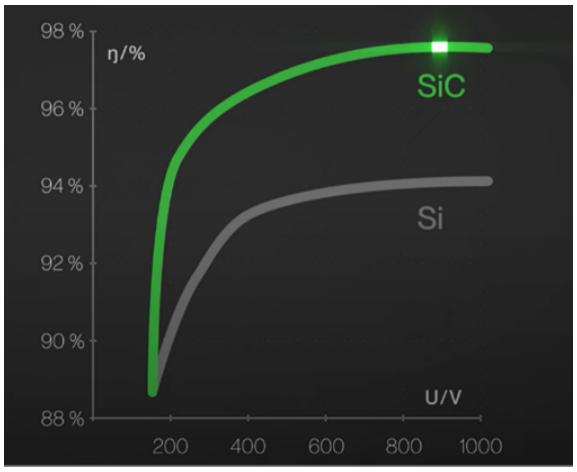

Figure 3.9: Efficiency curve of HYC400.

[2] *Alpitronic GmbH*, a company based in Italy specializing in high-performance EV chargers.

3.3 Charging pattern

For lithium-ion batteries, how fast the charging and discharging can proceed depends on reactions within the battery cells. These reactions are related to the charge transfer and the mass transport of the active species in the battery cells, which limit the charge rates of a battery. Most cell reactions have different time constants depending on the chemical constraints. The charge-transfer process at the electrode surface is fast (happening in seconds), but the mass transport is relatively slow (in the range of minutes or hours) and continues until all active species have been transformed. The slow mass-transfer reactions are the reason why cells can deliver or accept very high pulsed currents, but much lower continuous currents. If the charging rates are faster than the chemical reactions, they may cause local overcharge conditions, polarizations, or a local temperature rise, which can damage the battery. It is necessary to introduce rest periods during the charging procedure in order to give the mass transport reactions time to proceed to equilibrium. Another risk of charging the battery at a too fast rate is that side reactions may take place instead of the main reactions, jeopardizing the durability and safety of the battery. To avoid these problems, it is necessary to charge the batteries with the right strategy to avoid safety issues and damage to battery health while simultaneously charging the battery as fast as possible[10].

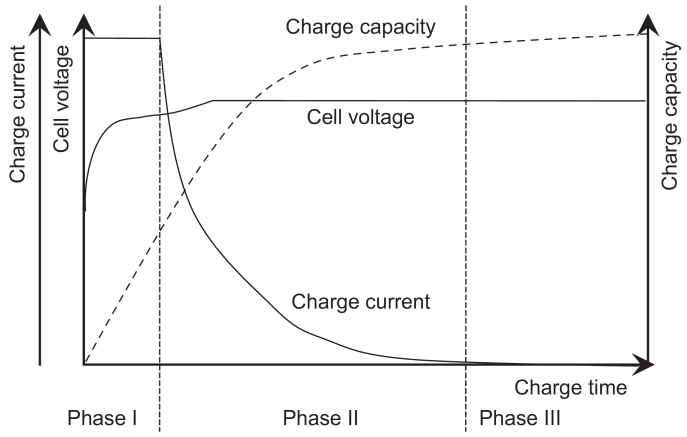

Figure 3.10: The Constant Current-Constant Voltage (CC-CV) charging pattern.

In this study, for fast charging the EV, the constant current-constant voltage method is used. This charging method is one of the common charging methods suitable for fast charging of Li-ion batteries and avoids damaging conditions. The charging procedure can be divided into different phases. Phase I refers to the maximum current flow time period. When the voltage limit has been reached, the current drops gradually to a minimum level, which is Phase II. In this phase, the battery is charged by the voltage-controlled procedure, and the current declines to a minimum level as the voltage approaches a fully charged state. Lastly, Phase III refers to a period of low current flow in the cell, which compensates for the normal self-discharge occurring in all cells. Phase III also allows the chemical reactions to reach a long-lasting equilibrium. A low current is applied until a predefined minimum current

level is reached and the charging current is interrupted. Increasing the charging current will not necessarily shorten the charging time. Figure 3.10 illustrates this charging method and its corresponding phases[10].

3.4 Simulation and modeling approach

In this study, simulations are conducted in three main stages, (Figure 3.11). In the first stage, the heat generation rate at the EV inlet is calculated by simulating the electrical contact. This calculation is performed using COMSOL Multiphysics, and the result is used as an input in the next stage. In the second stage, 3D thermal simulations are conducted for selected charging cable structures by utilizing CFD analyses in StarCCM+. The outcomes of this stage include the cooling demand and energy loss for each charging cable structure, which are then used in the final stage to investigate the charging system's performance in various scenarios. The final stage involves 1-D thermal simulations of the charging system (charging cable and power modules) in Simulink to evaluate the overall system performance under various thermal management strategies.

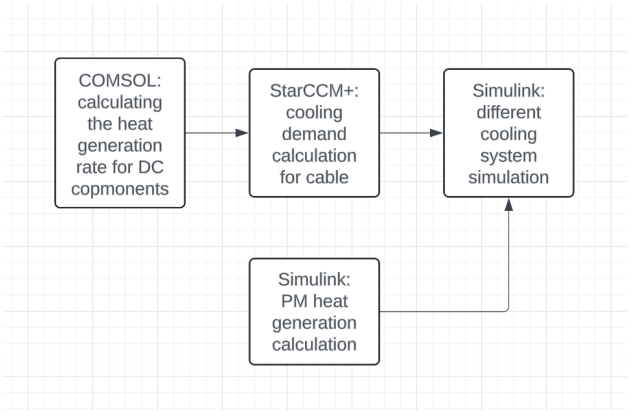

Figure 3.11: Simulation stages.

3.4.1 COMSOL simulations

In addition to Joule heating, there is another source of heat in the charging cable due to electrical contact resistance. The rate of heat generation at these points depends on factors such as the electrical current, conductor material, geometry, surface roughness, and the force applied between the contacting surfaces.

In [11], empirical tests were conducted to measure the contact resistance between two copper plates as a function of the applied pressure. Figure 3.12 shows the test setup used in this study, along with the current density lines during the test. The results, as depicted in Figure 3.13, provide the electrical contact resistance at the contact points for various applied pressures.

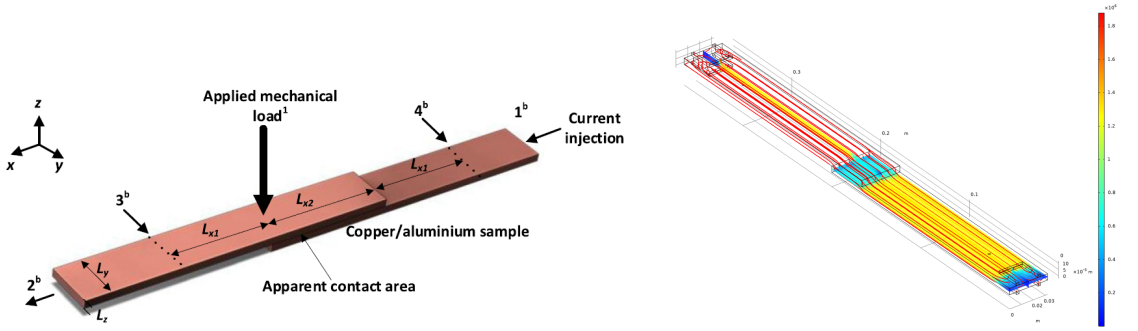

Figure 3.12: Contact resistance test: (a) Test setup, (b) Current density [A m^{-2}].

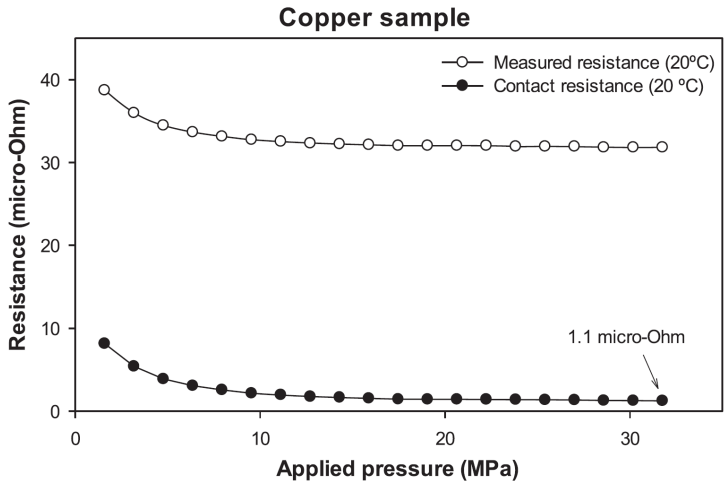

Figure 3.13: Resistance of a copper sample as a function of applied pressure.

In this study, to calculate the heat generation rate at the contact points, a simulation is conducted using COMSOL Multiphysics, addressing both Joule heating and electrical contact resistance. The simulation begins by developing a model for the connection point at the EV inlet, including the DC pin at the charger connector and the EV inlet, to consider the effect of geometry on thermal resistance. Figure 3.14 shows the model developed for the simulation. The contact resistance of the model is set based on the results from [11]. In this reference, the contact resistance for copper is provided as a function of applied pressure.
CharIN recommends in [1] that MCS connectors follow a 100 N force for insertion and removal, which is relatively low to ensure ease of use. As a rough estimate, 1 MPa is considered to be the pressure applied at the contact point. Based on Figure 3.13, the contact resistance in the simulation is set to 9 micro-ohms.
Other parameters used in the simulation are as follows:

- Material: Copper
- Initial temperature: 20°C
- Current: 1000 A

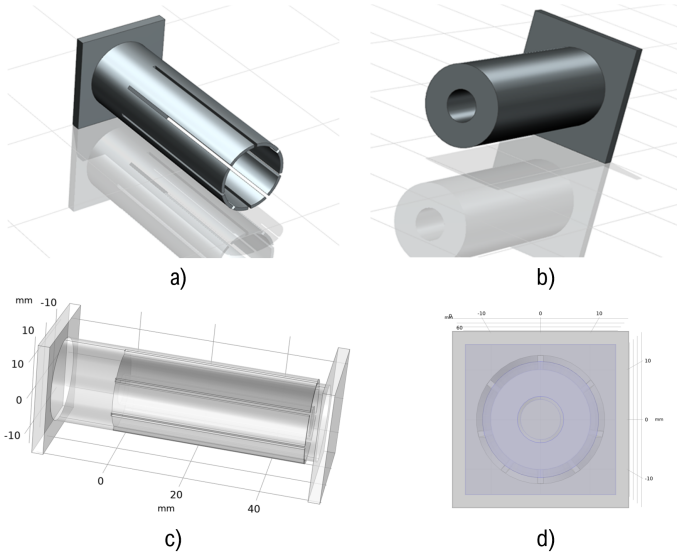

Figure 3.14: COMSOL model, (a) EV inlet, (b) Charger DC pin, (c) connection point (side view), (d) connection point (front view)

3.4.2 CFD simulations

CFD simulations are conducted to predict the thermal behavior of the chosen charging cables within the EV charging system. For each charging cable structure, the simulations are conducted in two stages. In the first stage, the cables are simulated under harsh working conditions—20 minutes of operation at maximum power—to determine a suitable mass flow rate for the coolant and to validate the functionality of the cable designs by ensuring that the cable temperatures remain within acceptable limits. With the coolant mass flow rates determined from the first stage, the second stage of simulations involves running the chargers under desired working conditions for 45 minutes following the CC-CV charging pattern. These simulations account for real-world operational conditions and provide data on the thermal management requirements of the system. The results of this stage, including energy loss and cooling demand, are used in the 1-D system simulations detailed in Section 3.4.3. The key inputs for the CFD models include:

- Charging cable models developed in Section 3.2.1.
- Ambient temperature.
- Charging pattern.
- Heat generation rates within DC pins, as calculated in Section 3.4.1.
- Thermal properties of the materials.
- Maximum allowable temperatures, as specified by CharIN in [1].

Using these inputs, and after setting up and solving the model with CFD techniques, the following outcomes are obtained:

- Cooling demand of the coolant.
- Mass flow rate of the coolant.

- Heat dissipation to the environment.
- total energy loss in the cable.

3.4.2.1 Model preparation

Based on the designs presented in Section 3.2.1, three CFD models were developed to analyze the thermal behavior of the chosen cable structures. Each model represents a charging cable with a total length of 220 cm, including the connector and EV inlet. To investigate the effect of ambient conditions on the heat dissipation of the cables, the models are considered in a large room with dimensions of 1.2 m x 5 m x 6 m, simulating a natural convection environment without wind, (Figure 3.15). The models are divided into five regions: Ambient, Insulation, DC conductors, DC pins, and Coolant, which are described below.

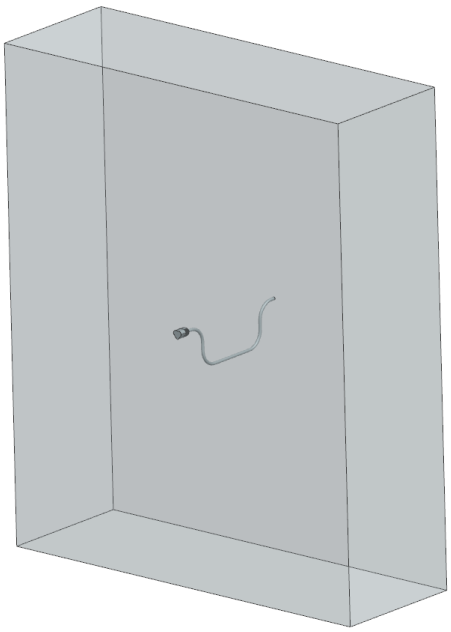

Figure 3.15: CFD model of the charging cable and ambient environment.

- Ambient

The ambient region in the model is defined as a cubic room, representing the surrounding air environment. The material properties for this region are assigned using the predefined air properties available in the StarCCM+ database. The initial temperature of the ambient air is set to 25°C. The outer boundaries of the ambient region consist of six walls, which are set to constant temperature boundaries at 25°C to maintain the thermal stability of the environment. The interfaces between the ambient region and the cable are treated as coupled boundaries, allowing heat transfer between the air and the cable surfaces.

- Insulation

This region represents the insulation, filler, and sheath materials of the cables. The material properties for this region are set according to the values in Table 3.3. The boundaries at the start and end of the cable models, where the insulation interfaces with the ambient room walls, are modeled as adiabatic walls. All other boundaries within the insulation region are treated as coupled boundaries, allowing heat transfer at the interfaces with adjacent regions.

- DC conductors

The DC conductor region represents the copper conductors within the cables, which serve as the primary source of heat generation. The heat generated in this region is governed by Ohmic loss, as described by Equations 2.14 and 2.17, which relate heat generation in copper to the temperature and current. Additionally, the time-dependent current profile, as shown in Figure 3.10, is used to define a field function that calculates the heat generation within the conductors as a function of both temperature and time.

The material properties for this region are specified as copper, utilizing the pre-defined data available in the software database. The boundary at the start of the cable models, where the conductor interfaces with the ambient room wall, is modeled as adiabatic walls. All other boundaries within this region are treated as coupled boundaries, allowing for heat transfer at the interfaces with adjacent regions.

- DC pins

This region represents the interface between the charger and the EV inlet, where the DC pins are located. Heat generation in this region is influenced by both Ohmic loss and electrical contact resistance loss. These losses are calculated in Section 3.4.1 and are integrated into the model as a field function, which uses the results from that section along with the charging pattern provided in Figure 3.10.

Similar to the DC conductors, the material for this region is specified as copper, using the software database. All boundaries within this region are treated as coupled boundaries to allow heat transfer at the interfaces with adjacent regions.

- Coolant

The coolant region features three types of boundaries. The **Inlet Boundary** is where the coolant enters the system, with the inlet temperature set to 25°C. The mass flow rate is specified at this boundary to initiate the coolant flow. The **Outlet Boundary** allows the coolant to exit the region after circulating through the system. The **Interface** facilitates heat transfer between coolant and adjacent regions. The coolant properties vary depending on the type of cable used. Table 3.4 shows the coolant properties used for each cable type.

Table 3.4: Coolant properties for different cable types [3]

Property	Cable types one and two	Cable type three
Material	35% mass glycol-water mixture	Mineral oil
Density	1050 kg/m^3	870 kg/m^3
Dynamic Viscosity	0.003 Pa · s	0.01 Pa · s
Specific Heat	3600 J/kg · K	2000 J/kg · K
Thermal Conductivity	0.55 W/m · K	0.136 W/m · K
Prandtl Number	0.9	0.9

3.4.2.2 Simulation model configuration

Table 3.5 summarizes the CFD model setup used for each continuum in the simulation. Each aspect of the setup is described below.

Table 3.5: CFD model setup overview

	Air	Coolant	Copper	Insulation
Space	Three Dimensional			
Time	Implicit Unsteady			
Equation of State	Constant Density			
Gradient	Enabled			
Material	Gas	Liquid	Solid	Solid
Energy	Coupled Energy		Coupled Solid Energy	
Flow	Coupled Flow		-	-
Viscous Regime	Turbulent (RANS)		-	-
	Realizable k-ϵ		-	-
Wall Treatment	Two layer all Y+		-	-
	Wall distance		-	-
Buoyancy	Boussinesq		-	-
	Gravity		-	-

- Spatial and temporal configuration

The simulations are set up in a three-dimensional space. Transient time frames are used to account for changes over time rather than assuming a steady-state condition.

[3] Values are provided at SATP conditions (25°C and 1 atm).

- Equation of state

All materials are assumed to have constant density. Since temperature variations do not cause significant changes in the material densities, this assumption simplifies the simulation and reduces the computational complexity.

- Gradient model

The gradient model is employed to calculate the gradients in temperature and velocity fields. This model ensures the accurate capture of heat transfer and flow characteristics within the different continua. It supports the coupled simulation models by ensuring that temperature and flow properties are resolved with sufficient detail.

- Energy model

Coupled energy models are used to simulate heat transfer. This model allows for the simultaneous solution of energy and momentum equations among the different materials.

- Flow and turbulence modeling

To simulate the airflow caused by natural convection around the cable and the coolant flow inside the cable, coupled flow models are implemented. The flow is assumed to be in a turbulent regime, modeled using the Reynolds-Averaged Navier-Stokes (RANS) equations. Turbulence is modeled using the Realizable k-epsilon turbulence model, which is suitable for handling the turbulent mixing of air and coolant.

- Near-wall treatment

Near-wall treatment models are a set of semi-empirical functions designed to accurately capture the physics of flow in the near-wall region. Turbulence is significantly influenced by the presence of walls, primarily due to the no-slip condition that must be satisfied at the wall surface. To improve accuracy in regions close to the walls, the "Wall Distance" and "Two-Layer All y+ Wall Treatment" models are employed. These approaches adjust the near-wall treatment based on mesh resolution, thereby enhancing the consistency and accuracy of the simulation results.

- Buoyancy and natural convection effects

The Boussinesq model is used to simulate natural convection effects caused by temperature differences within the air continuum surrounding the cable. This model approximates density variations as a function of temperature differences, providing a simplified yet effective representation of buoyancy-driven flows. Additionally, gravity is included in the simulation to account for the buoyancy forces that drive natural convection around the cable.

3.4.2.3 Mesh generation

In this study, mesh generation is performed using StarCCM+'s built-in meshing tools. In CFD studies, mesh generation is an important step as it directly impacts the accuracy and computational efficiency of the simulations.

The process starts by imprinting the parts together in StarCCM+. For the solid parts (insulation and conductors), the meshing process is done using the **"Surface Remesher"** and **"Polyhedral Mesher"** tools to refine and prepare the surface mesh and to create the volume mesh. For the fluid parts (coolant, air), in addition to the mentioned tools, the **"Prism Layer Mesher"** is applied to resolve the boundary layer effects near solid boundaries. The prism layers are used to capture the steep gradients in velocity and temperature that occur near solid boundaries.

To reduce the computational cost, it is necessary to set the resolution of the mesh strategically in the model. Therefore, the mesh is refined in areas where high thermal gradients are expected, such as the interior of the cables and the ambient region around it. These regions require higher mesh density to capture the heat generation and dissipation accurately. Conversely, the mesh is coarsened in regions with lower activity, such as the ambient area far from the cable. This approach reduces the overall cell count and computational costs while maintaining accuracy.

The mesh setup for each model is tuned to achieve an average Y+ in the range of 1 to 5. This range is optimal for the near-wall treatment functions set in the previous section. To ensure that the results are mesh-independent, a mesh sensitivity study is conducted. The study involved comparing the simulation results using both coarser and finer meshes to ensure that the final mesh setup provided accurate results without being overly refined, which would unnecessarily increase computational costs.

Figure 3.16 shows a cross-sectional view of the mesh for Model Type Two. Tables 3.6, 3.7, and 3.8 summarize the final mesh parameters used for the solid regions, ambient air, and coolant, respectively.

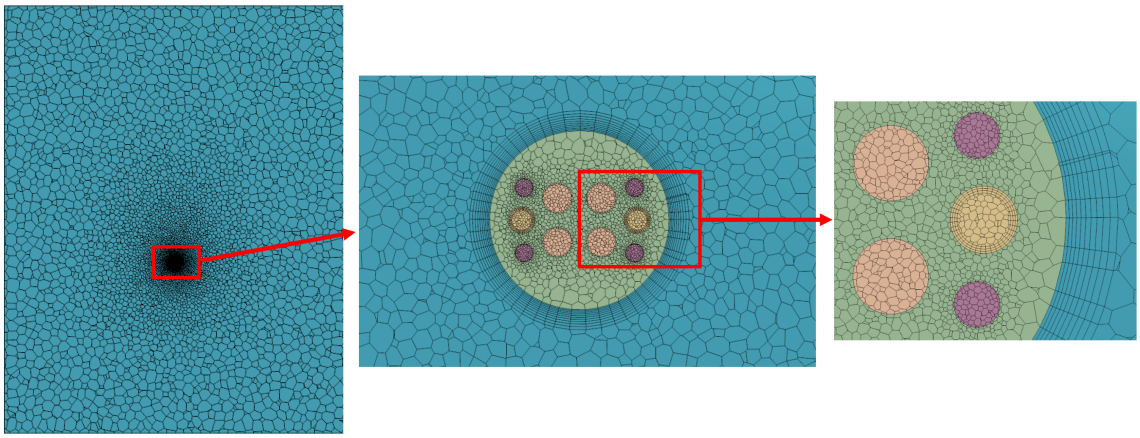

Figure 3.16: Cross-sectional view of the mesh for cable Type Two.

Table 3.6: Meshing parameters for the conductor and insulation Regions.

Parameter	**Value**
Base Size (mm)	1
Minimum Surface Size (mm)	0.1
Target Surface Size (mm)	1
Volume Growth Rate	1.2
Surface Growth Rate	Default

Table 3.7: Meshing parameters for the ambient region.

Parameter	Value
Base Size (mm)	1
Minimum Surface Size (mm)	0.1
Target Surface Size (mm)	50 (Type 1), 100 (Type 2), 75 (Type 3)
Volume Growth Rate	1.05 (Type 1), 1.04 (Type 2), 1.03 (Type 3)
Number of Prism Layers	10
Prism Layer Thickness (mm)	5.6
Surface Growth Rate	Slow
Prism Layer Stretching	1.14 (Type 1), 1.1 (Type 2 and 3)

Table 3.8: Meshing parameters for the coolant region.

Parameter	Value
Base Size (mm)	1
Minimum Surface Size (mm)	0.1
Target Surface Size (mm)	1
Volume Growth Rate	1.2
Number of Prism Layers	3 (Type 1 and 2), 2 (Type 3)
Prism Layer Thickness (mm)	0.76 (Type 1), 0.75 (Type 2), 1 (Type 3)
Surface Growth Rate	Default
Prism Layer Stretching	1.14 (Type 1), 1.1 (Type 2 and 3)

3.4.3 System simulation in MATLAB Simulink

One-dimensional simulations are conducted using MATLAB Simulink, along with the Simscape library, to model the thermal management of the charging system. The simulations include the MCS power cabinet, which houses ten 100 kW power modules, as well as the charging cable. The simulations are carried out in four stages which are described in the following sections. The stages include:

- **Stage 1:** SOC calculation
- **Stage 2:** Heat generation calculation
- **Stage 3:** Power module thermal mass simulation
- **Stage 4:** Cooling systems simulations

The inputs of the simulations include:

- CC-CV charging pattern (Stage 1)
- EV battery and charge parameters (Stage 1)
- Power module's efficiency curve (Stage 2)
- Charging cable cooling demand (Stage 2)
- Power module specifications (Stage 3)
- Ambient conditions (Stage 4)
- Cooling systems' equipment specifications (Stage 4)

The outputs of the simulation are:

- Total energy loss in the power modules
- Power module temperature over time
- Energy consumption for each cooling system
- Overall efficiency of the charging system

3.4.3.1 SOC calculation

In this part of the simulation, the power intake of the electric vehicle (EV) and the output voltage and current of the power module are calculated over time. These calculations are used to assess both the heat generation and efficiency of the power module.

Figure 3.17 illustrates the Simulink model used for SOC calculation. In this model, the charging pattern shown in Figure 3.10 provides the current, voltage, and state of charge (SOC) over time. These curves are incorporated into the model using three Lookup Table modules. The x-axis of the curve is divided into 2700 time steps, representing a total charging duration of 45 minutes. One Lookup Table determines the time (with output values ranging from 0 to 2700) based on the SOC value. The other Lookup Tables provide the voltage and current values (scaled between 0 and 1). The maximum values of voltage and current from the curve are used as the system's peak values. In the SOC curve, the initial SOC is set to 20% and the final

SOC to 80%.

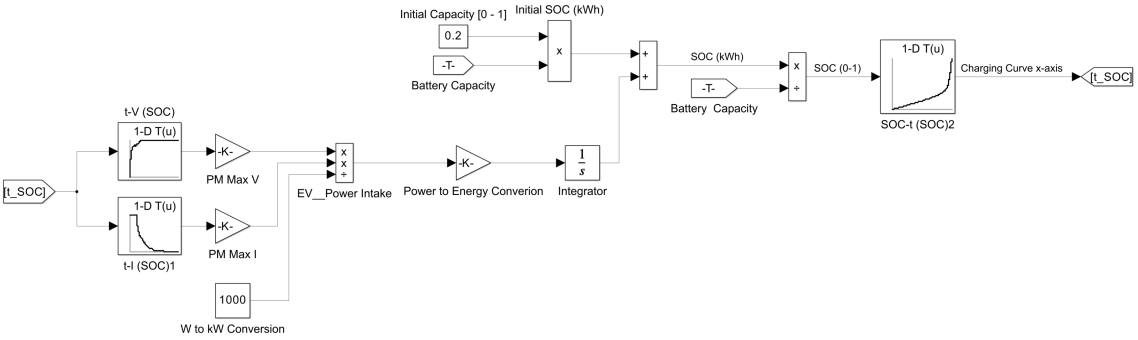

Figure 3.17: Simulink model of SOC calculation using the CC-CV pattern.

The SOC calculation model follows this algorithm:

- **Step 1:** Compute the initial stored energy in the battery (in kWh) based on the initial SOC (20%) and the battery capacity (600 kWh).
- **Step 2:** Calculate the SOC at each time step.
- **Step 3:** Use the first Lookup Table to determine the time.
- **Step 4:** Retrieve voltage and current values from the other Lookup Tables. Multiply these scaled values by the maximum voltage and current to obtain actual voltage and current over time.
- **Step 5:** Calculate the EV's power intake over time using the obtained voltage and current values.
- **Step 6:** Divide the power intake by 3600 to convert it to energy stored during each time step (in kWh).
- **Step 7:** Update the battery's stored energy by integrating the energy added during each time step.
- **Step 8:** Repeat the process from Step 2 until the SOC reaches 80%.

3.4.3.2 Heat generation computation

In this part of the simulation, the heat generation of the power module is calculated over time to serve as the input for the power module cooling system simulations. Additionally, the cooling demand of the charging cable, derived from the results of CFD simulations, is incorporated into the model to be used as the input for the charging cable cooling system.

Power module

The calculation of heat generation is performed using the power module efficiency provided by the manufacturer as shown in Figure 3.9. This curve provides the efficiency of the power module as a function of its output voltage. Figure 3.18 illustrates the Simulink model for the power module heat generation calculation.

In the model, the power module efficiency curve (Figure 3.9) is utilized as a Lookup Table module to determine the efficiency at each time step. With the intake voltage

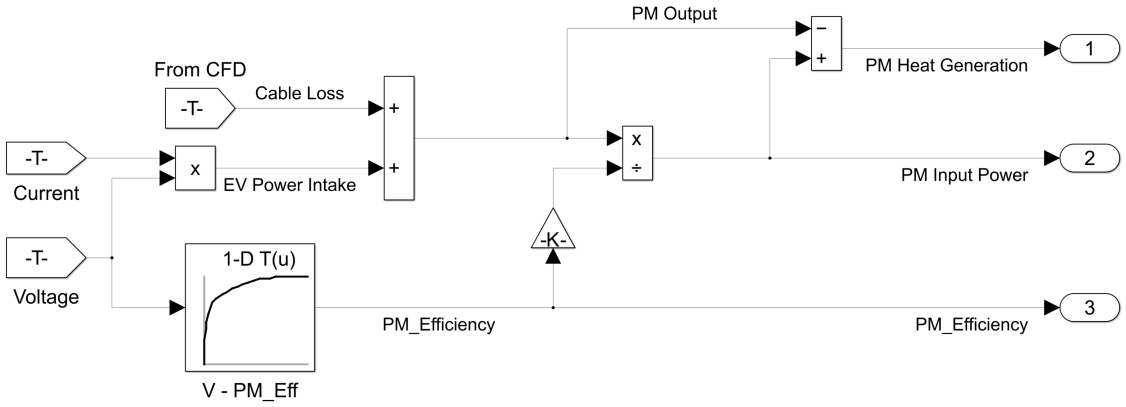

Figure 3.18: Simulink model for power module heat generation.

and current known from the previous section, the EV's power intake is calculated as shown in Equation 3.5. The power module's output power is then determined by summing the EV power intake and the charging cable loss power (obtained from CFD simulations), as indicated in Equation 3.6. The power module's input power is subsequently calculated by dividing the output power by the efficiency, as shown in Equation 3.7. Finally, the power module's power loss—which represents the heat generated by the power module—is calculated by subtracting the output power from the input power, as shown in Equation 3.8.

$$P_{\mathrm{EV}}(t) = V(t) \times I(t) \tag{3.5}$$

$$P_{\mathrm{PM,\ output}}(t) = P_{\mathrm{EV}}(t) + P_{\mathrm{cable\ loss}}(t) \tag{3.6}$$

$$P_{\mathrm{PM,\ input}}(t) = \frac{P_{\mathrm{PM,\ output}}(t)}{\mathrm{Efficiency}_{\mathrm{PM}}(t)} \tag{3.7}$$

$$\dot{Q}_{\mathrm{PM}}(t) = P_{\mathrm{PM,\ input}}(t) - P_{\mathrm{PM,\ output}}(t) \tag{3.8}$$

Charging cable

The cooling demand of the charging cable models is incorporated into the Simulink model using the results of CFD simulations. For this, the mass flow rate of the coolant is multiplied by the coolant's specific heat and the difference between the coolant's output and input temperature over time, as shown in Equation 3.9.

$$\dot{Q}_{\mathrm{cable}} = \dot{m}_{\mathrm{coolant}} \times c_{\mathrm{coolant}} \times \Delta T_{\mathrm{coolant}} \tag{3.9}$$

3.4.3.3 Power module thermal mass simulation

In the one-dimensional system simulations, the power module is modeled as a lumped-element system, where the entire module is treated as a single thermal mass with uniform temperature and material distribution. Figure 3.19 illustrates this

concept. The power module is assumed to be composed of three primary materials by mass: Copper (50%), Silicon (30%), and FR4[3] (20%).
These materials were selected based on their prevalent use in power modules. Copper, due to its superior thermal and electrical conductivity, is extensively used in bus bars, connectors, and heat sinks. Silicon, a semiconductor material, is widely used in power electronics. FR4 serves as the base material in printed circuit boards (PCBs).

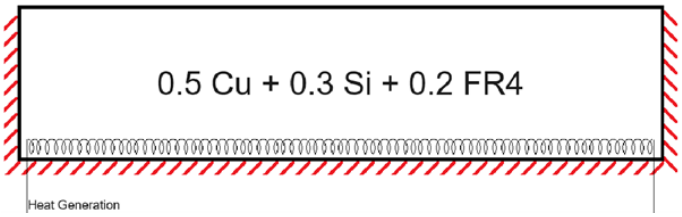

Figure 3.19: Thermal mass representation of the power module.

Figure 3.20 shows the Simulink model for the power module. In this model, a Thermal Mass module represents the power module. Heat generated within the power module is applied to the Thermal Mass module through an external heat source, and the power module's temperature is managed by the thermal management systems connected to it.

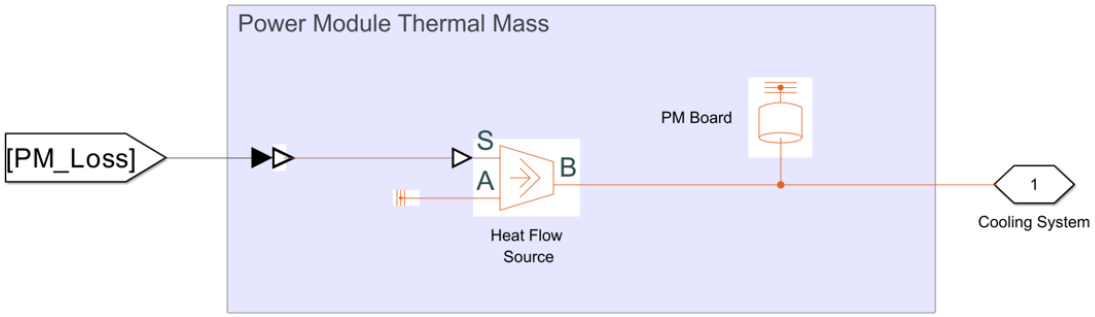

Figure 3.20: Simulink model of the power module as a thermal mass.

3.4.3.4 Thermal management system models

This section details the thermal management system models used to dissipate heat generated by the power modules and charging cables. Four different cooling systems are implemented to evaluate their performance and effectiveness in maintaining optimal temperatures within the power modules:

- Heatsink
- Heatsink + Phase Change Material (PCM)
- Liquid Cooling

[3]FR4 is a composite material made from woven fiberglass and epoxy resin.

- Immersion Cooling

A modified version of the Liquid Cooling system is also employed to investigate the thermal management system for the charging cable. Each system is described in detail below.

Heatsink

The heatsink cooling system is a fundamental and widely implemented solution for managing heat in power electronics across various applications. The primary components of this system include a heatsink and a fan, as depicted in Figure 3.21. The heatsink facilitates heat transfer from the heat sources to its fins, while the fan induces forced ventilation by moving air over the fins, thereby dissipating the excess heat into the ambient environment through convection.

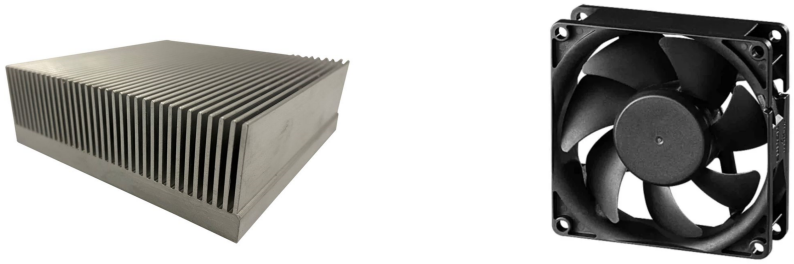

a) b)

Figure 3.21: Heatsink cooling system components: (a) Heatsink, (b) Fan.

Figure 3.22 illustrates the Simulink model of the heatsink cooling system. In this model, heat dissipation occurs through two primary mechanisms: (1) forced ventilation and (2) natural convection.

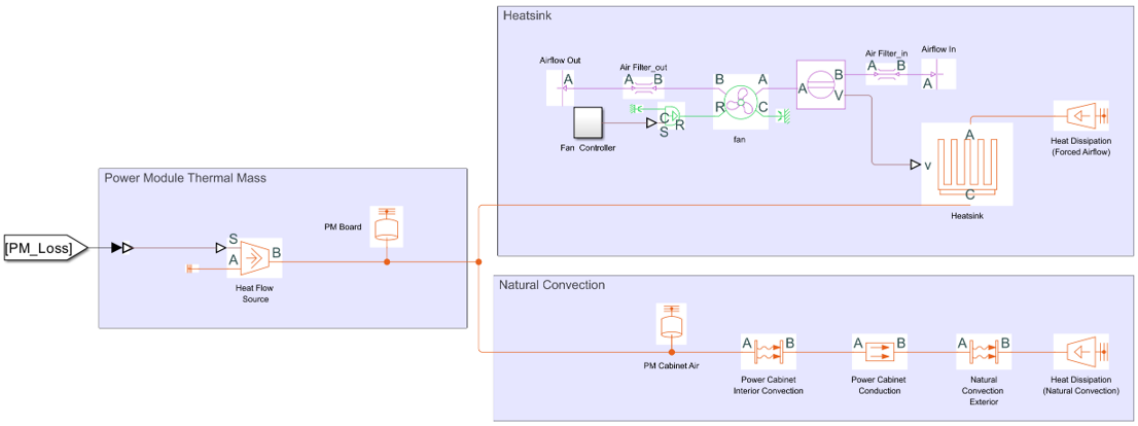

Figure 3.22: Simulink model of the heatsink cooling system.

1. Forced Ventilation: In the forced ventilation pathway, heat is transferred from the power module's thermal mass to the heatsink. The fan module draws ambient air through a flow resistance unit (which represents an air filter), then passes the

air over the heatsink fins, facilitating heat dissipation. After absorbing heat, the air exits through another flow resistance unit before being released into the ambient environment.
The heatsink parameters are set based on the datasheet for the model "62335," with 100 heatsinks utilized to cover one side of 10 HYC400 power modules. The fan is modeled according to the "PD150B-220" datasheet, with a total of 40 fans employed to manage the cooling load. A three-speed controller, depicted in Figure 3.23, modulates the fan speed. The controller compares the power module's temperature with the maximum allowable limit (set at 80°C). Depending on the temperature difference, the controller activates zero, one, two, or all three relays, each outputting a signal to adjust fan speed. A Lookup Table uses the relay outputs to determine the fan speed. Additionally, a delay module and a transfer function block are included in the model to simulate the dynamic response characteristics of the fan under real-world conditions. Technical details of the components used in the model, including the heatsink, fan, and air filter, can be found in Appendix B.

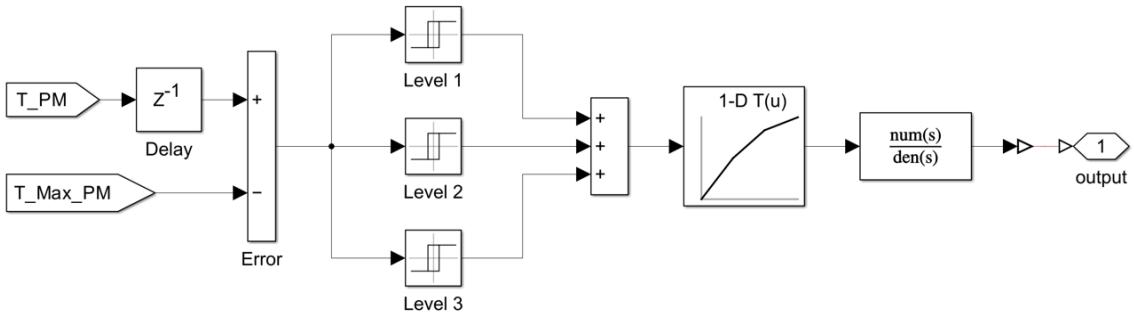

Figure 3.23: Simulink model of the three-speed fan controller.

2- Natural Convection: In the natural convection pathway, the static air within the power cabinet is modeled as a thermal mass. Heat is transferred by convection from the power module to the interior surfaces of the power cabinet. This heat then conducts through the cabinet walls and dissipates to the ambient air via natural convection.

Heatsink + PCM

This cooling system builds upon the Heatsink cooling system model by incorporating a Phase Change Material (PCM). The addition of the PCM module introduces a material that absorbs and releases heat during phase changes, specifically designed to operate within the temperature range of the system. PCM materials are effective in moderating temperature fluctuations by absorbing significant amounts of heat when they undergo phase changes, thereby acting as a thermal buffer. This results in a reduced rate of temperature rise within the system, helping to maintain lower operating temperatures.
The PCM's effectiveness is limited to the duration until the material completes its phase transition. Therefore, this approach is particularly suitable for systems

experiencing occasional peaks in temperature rather than those with continuous, high-temperature operations.
Table 3.9 presents the parameters set for the PCM used in the model, which is paraffin, and Figure 3.24 displays the modified Simulink model incorporating the heatsink and PCM.

Property	Value
Mass	10 kg
Specific Heat	730 J/(K.kg)
Latent Heat	210 kJ/kg
Melting Temperature	58 °C
Initial Fraction of Solid	1 [0,1]

Table 3.9: Set parameters for the PCM material, Paraffin.

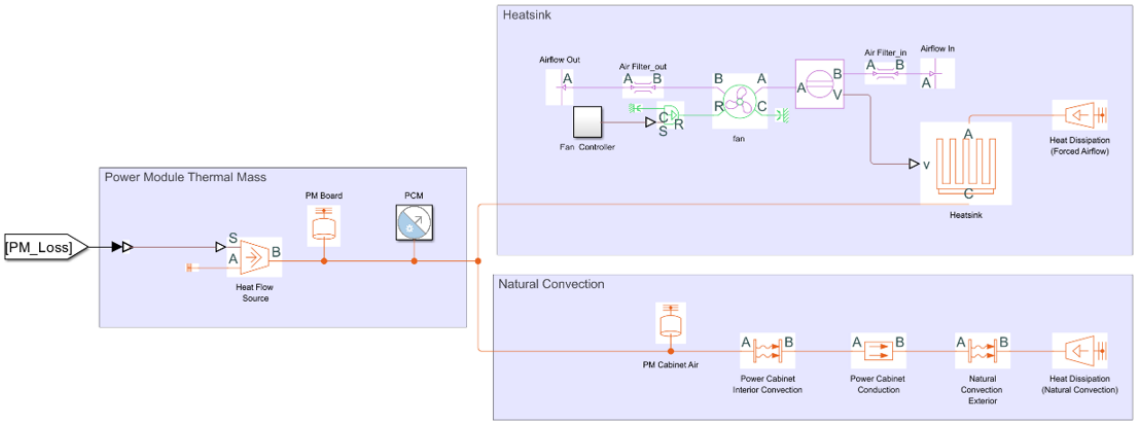

Figure 3.24: Simulink model of the heatsink with PCM cooling system.

Liquid cooling

In the liquid cooling system, excess heat from the power modules is managed using cold plates attached to them, (Figure 3.25). These cold plates absorb heat from the power modules and transfer it to a circulating coolant. The coolant carries the heat away from the cold plates and releases it into the ambient environment through a dry air cooler.

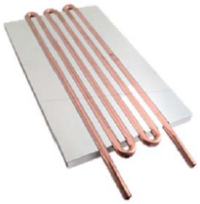

Figure 3.25: Cold plate used in the liquid cooling system model.

Figure 3.26 illustrates the Simulink model for the liquid cooling system. Similar to previous cooling systems, the model accounts for heat dissipation through natural convection. In this setup, the cold plates are modeled using a thermal mass, which simulates the aluminum base, and a variable thermal resistance that represents the heat transfer through the coolant. The thermal resistance of the cold plates decreases as the coolant flow rate increases, as shown in Figure B.4.

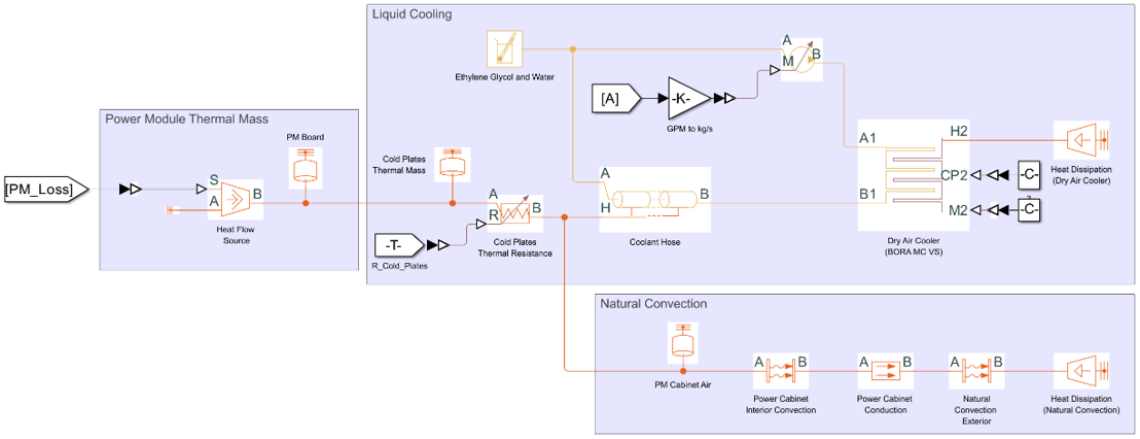

Figure 3.26: Simulink model of the liquid cooling system.

The parameters for the cold plates are derived from the BOYD 6-pass cold plate datasheet, (see Apendix B). In the model, 100 cold plates are arranged in parallel to cover one side of the power modules.
A three-speed controller (shown in Figure 3.27) adjusts the total thermal resistance of the cold plates. This controller compares the temperature of the power modules to the maximum allowable temperature and determines the coolant flow rate accordingly (similar to the approach used in the heatsink model), then the thermal resistance of each cold plate is calculated using a Lookup table module, (Figure B.4). Since the cold plates are considered to be installed in parallel the total thermal resistance of the cold plates is then determined by dividing this value by the number of cold plates.

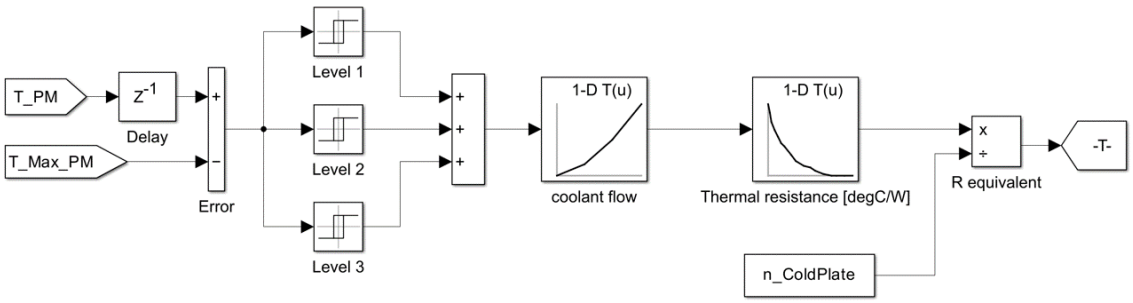

Figure 3.27: Simulink model of the cold plate controller.

Heat absorbed by the cold plates is transferred to a pipe containing a glycol-water mixture with a 34% volume fraction. This mixture is cooled by a heat exchanger module, representing a dry air cooler. The parameters for the dry air cooler are

based on the technical specifications of the "BORA MC VS 1000.80-1/1L.E-2 (see Appendix B."

* To investigate the thermal management system of the charging cable, a modified model based on the liquid cooling system is considered. In this model, instead of using variable thermal resistance, the cooling demand of the charging cables, as calculated in Section 3.4.3.2, is directly added to the coolant hose. The heat exchanger parameters are also adjusted based on a smaller cooler, specifically the OAC 100 cooler (see Appendix B), to match the reduced cooling capacity requirements of the charging cable.

Immersion cooling

In the immersion cooling system, the power modules are immersed in a dielectric medium that serves as the coolant. The heat generated by the power modules is transferred to the coolant, which then dissipates the heat to the ambient environment through an oil/air cooler. Figure 3.28 shows the Simulink model of the immersion cooling system.
As in previous cooling systems, heat dissipation through natural convection is considered in the model. The excess heat from the power modules is transferred to a tank module containing the coolant. The coolant parameters are derived from the FC-3283 dielectric coolant datasheet (see Appendix B). A heat exchanger module represents the oil/air cooler, with parameters set according to the product datasheet of the OAC-400 (see Appendix B). A controller, similar to the one used in the heatsink system, regulates the flow rate of the coolant pump.

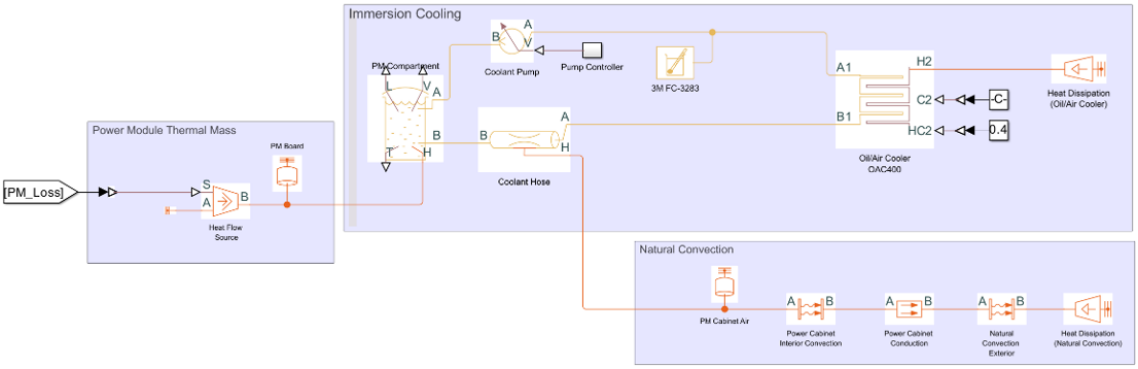

Figure 3.28: Simulink model of the immersion cooling system.

4
Results

This chapter presents the simulation results obtained from the thermal analysis of the EV charging system. The first section focuses on the 3D simulation results for three different types of EV charging cables. The second section provides results from the 1D thermal management studies of the overall system.

4.1 3D simulation results of EV charging cables

This section presents the thermal simulation results for the EV charging cables. First, the results from COMSOL simulations are provided, showing the heat generation rate for the connection pin at the EV inlet. Following this, the CFD simulation results for the three selected cable structures are discussed under extreme operating conditions (20 minutes at maximum load) to validate their functionality. Finally, the CFD simulation results for these cable structures are presented under normal operating conditions using a Constant Current-Constant Voltage (CC-CV) charging pattern over a 45-minute duration.

4.1.1 COMSOL simulation results

A 3D simulation is conducted using COMSOL to investigate the heat generation for the connection pin at the charger and vehicle interface. Table 4.1 presents the heat generation rates at the vehicle inlet. The results indicate that the total heat generation rate, considering both the ohmic loss of the conductor and the electrical contact loss, is 5.83 W. In contrast, when only the ohmic loss is considered, the heat generation rate is 3.73 W.

Table 4.1: Power loss at the charger connection pin.

Condition	**Power Loss (W)**
Zero Contact Resistance	3.73
With Electrical Contact Resistance	5.83

Figure 4.1 illustrates the electric field distribution at the connection pin. The figure shows that without electrical contact resistance, the electric field follows a straightforward path, resembling a single conductor. In contrast, when contact resistance is present, the electrical pathway becomes more complex.

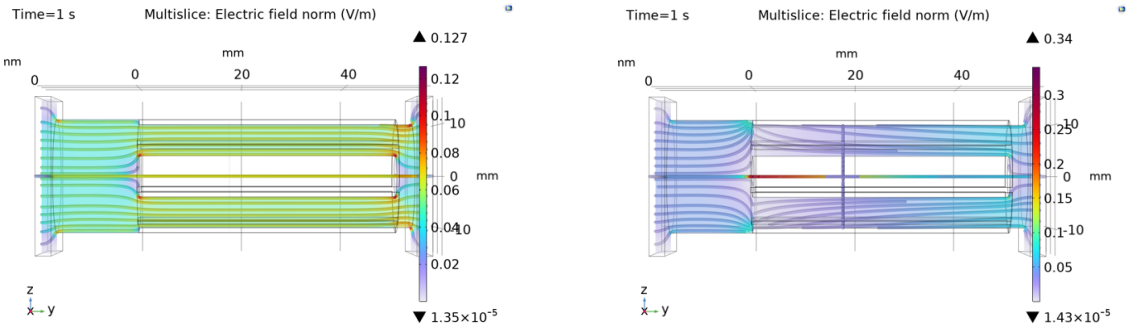

Figure 4.1: Electric field in the connection pin: (a) without contact resistance, (b) with contact resistance.

Figures 4.2 and 4.3 display the temperature distribution in the connection pin after one second under conditions of zero contact resistance and with contact resistance, respectively. The contours indicate a uniform temperature distribution when there is no contact resistance, whereas a hotspot is observed around the connection point in the presence of contact resistance.

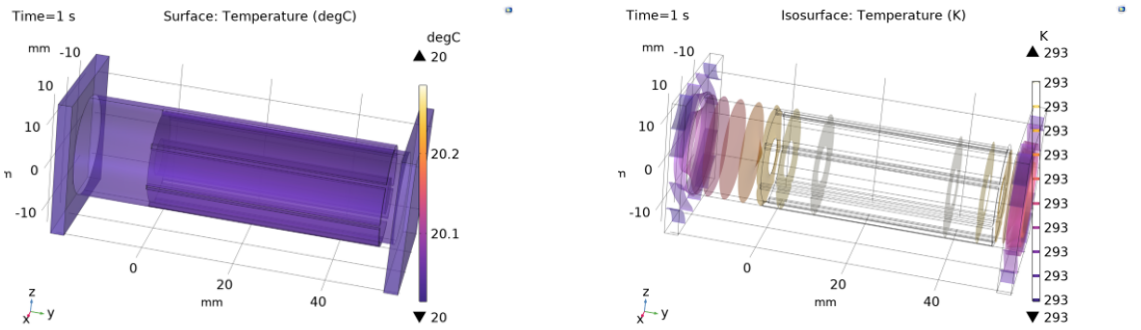

Figure 4.2: Temperature in the connection pin with zero contact resistance: (a) surface view, (b) isothermal view.

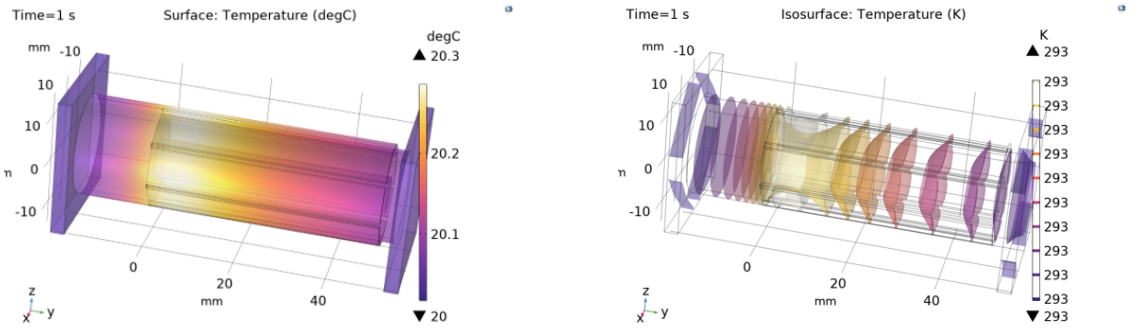

Figure 4.3: Temperature in the connection pin with contact resistance: (a) surface view, (b) isothermal view.

4.1.2 CFD simulation results

This section presents the CFD simulation results that evaluate the thermal performance of three EV charging cable designs under varying operating conditions. The three cable structures analyzed are:

- **Type 1:** Water-cooled cable with a copper-clad water channel design.
- **Type 2:** Water-cooled cable with a separate cooling channel design.
- **Type 3:** Oil-cooled cable.

The simulations investigate the thermal behavior of these designs under both extreme and normal operating conditions to assess their effectiveness in thermal management.

4.1.2.1 Extreme operating conditions

In the simulations, all three cables are evaluated under extreme operating conditions. Each cable is subjected to a maximum design output power of 1 MW, with operating parameters of 1000 V and 1000 A, for a duration of 20 minutes. The following graphs illustrate the temperature distribution and heat transfer rates over time for each cable type. Graphical results, including temperature and heat transfer contours at the end of the 20-minute simulation, are presented in Appendix C.

These results demonstrate that the temperatures within the cables remain within the recommended operational ranges (as specified in Table 1.4), thereby validating the effectiveness of the cable designs in managing thermal conditions under extreme scenarios.

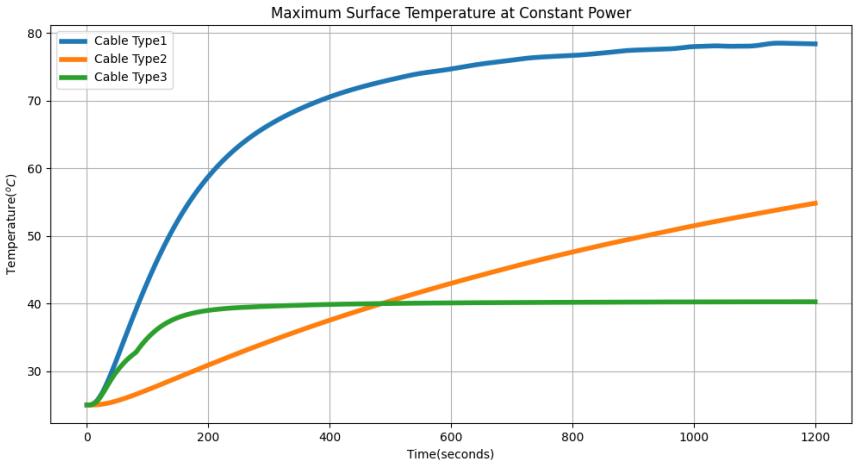

Figure 4.4: Maximum surface temperature under constant power.

Figures 4.4, 4.5, and 4.6 display the maximum temperatures recorded at each time step for the cable surface, DC conductors, and DC pins, respectively. The temperatures in all regions remain within the design limits. Among the three designs, Cable Type 3 achieves a steady state within the simulation period very fast. Its maximum surface temperature stabilizes at 40°C after 300 seconds, the DC conductor temperature peaks at 87°C after 200 seconds, and the DC pin temperature

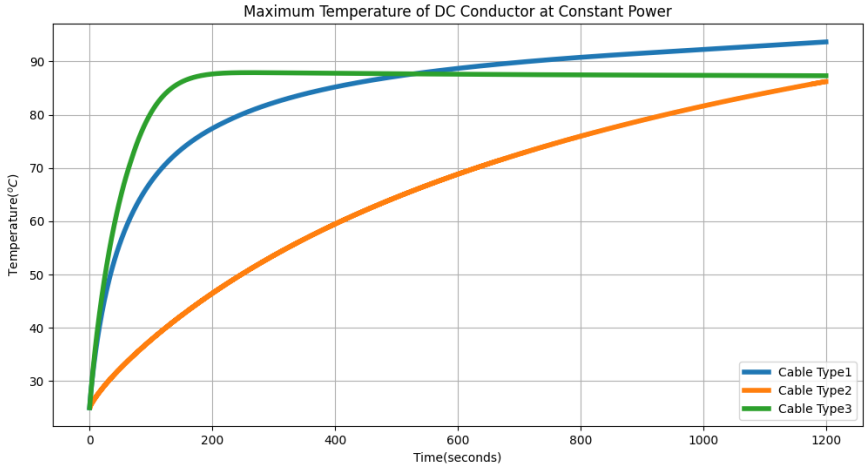

Figure 4.5: Maximum conductor temperature under constant power.

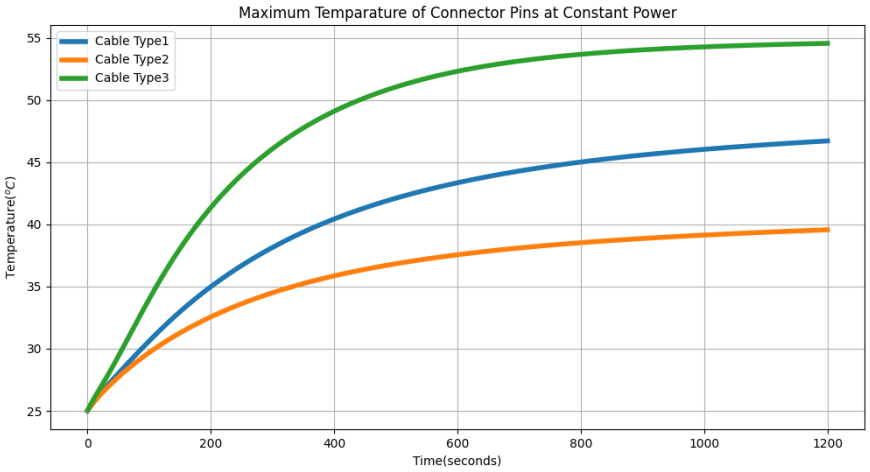

Figure 4.6: Maximum pin temperature under constant power.

reaches a maximum of 55°C after 20 minutes. This indicates that Cable Type 3 not only operates within safe temperature limits over the 20-minute period but is also unlikely to exceed these limits in prolonged operation.
The other cable types do not reach a steady state within the 20-minute period, but their temperature curves exhibit downward concavity, suggesting that they will likely stabilize within the temperature limits if given more time.

Figure 4.7 shows the coolant outlet temperature profile over the 20-minute operation period under constant power. The coolant outlet temperature is calculated as the mass flow average of the coolant cells at the outlet. In all cases, the coolant flow rate is maintained at 1.8 liters per minute and remains constant over time.

Figures 4.8 and 4.9 present the heat transfer rates from the charging cables to the coolant and ambient air, respectively. In Cable Type 3, the heat transfer rate to the coolant reaches its peak value quickly (after approximately 2 minutes), and the

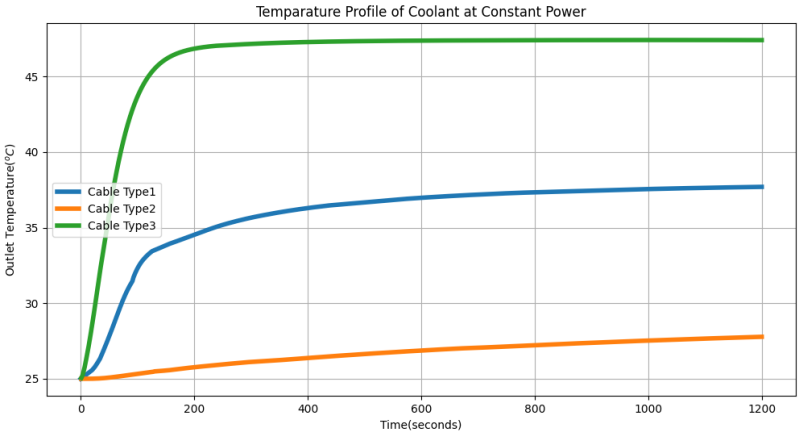

Figure 4.7: Coolant outlet temperature profile under constant power.

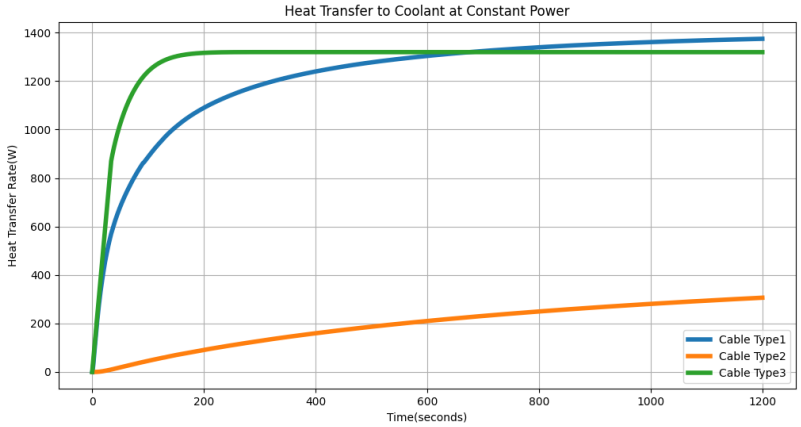

Figure 4.8: Heat transfer rate to coolant under constant power charging.

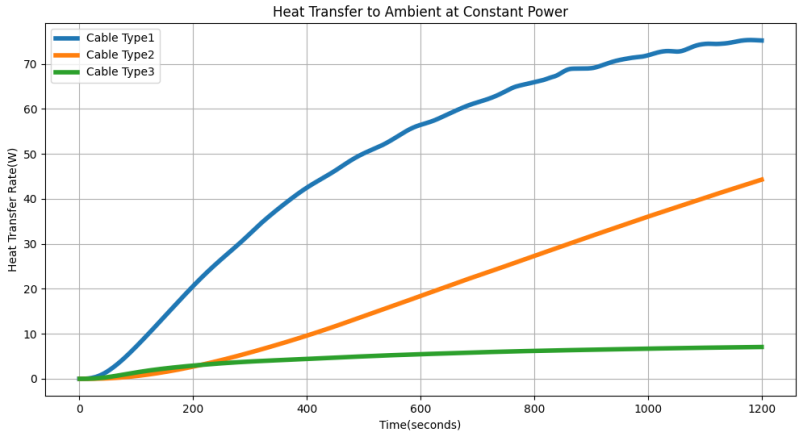

Figure 4.9: Heat transfer rate to ambient under constant power charging.

heat transfer rate to the ambient air is significantly lower compared to the other two cable designs. This is attributed to the design of Cable Type 3, where the coolant is closely integrated with the heat source, effectively trapping the heat within the coolant and minimizing dissipation through other paths. Consequently, the cooling system's efficiency in Cable Type 3 is higher than in the other designs.

4.1.3 CFD simulation results for CC-CV charging

This section presents the CFD simulation results for the cables under a CC-CV charging pattern over a 45-minute duration. Table 4.2 shows the total energy loss in the cables, and the following figures illustrate their thermal performance throughout the charging process.

	Energy Loss
Type 1	370 Wh
Type 2	128 Wh
Type 3	330 Wh

Table 4.2: Total energy loss in the cables under CC-CV charging.

As depicted in the figures, during the first phase of CC-CV charging—where the electric vehicle (EV) is charged under constant current—the heat transfer rate and temperatures increase. Following this phase, a significant drop in both parameters is observed. This is because at the end of the constant current phase (as shown in Figure 3.10), the current decreases drastically. Since the heat generation in the cables is proportional to the square of the current, this sharp current reduction leads to a steep decline in heat generation. Consequently, the heat transfer to the coolant and ambient air, as well as the cable temperature, rapidly decreases.

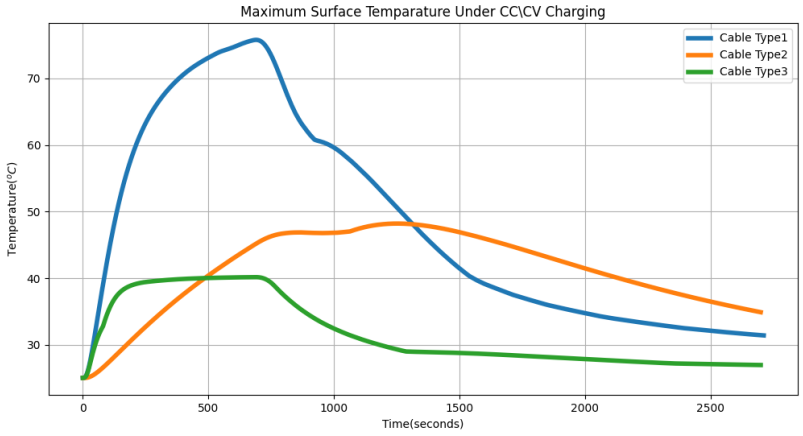

Figure 4.10: Maximum surface temperature under CC-CV charging.

Figure 4.10 shows the maximum surface temperatures of the cables. Cable Type 1, featuring a copper-clad water cooling design, records the highest surface temperature

of 74°C, significantly higher than the other cables. In this cable, the coolant flows through the center of the conductor, and a big share of the heat generated in the conductor dissipates outward, increasing the surface temperature. In contrast, Cable Type 2, which employs a separate cooling channel design, reaches a maximum surface temperature of 49°C. The lower temperature in Type 2 can be attributed to its larger conductor cross-sectional area, resulting in reduced heat generation and lower surface temperatures. Cable Type 3, which uses oil cooling, has the lowest surface temperature, with a maximum of 40°C. The efficient cooling in this design is due to the coolant surrounding the conductor, allowing heat to dissipate primarily through the coolant.

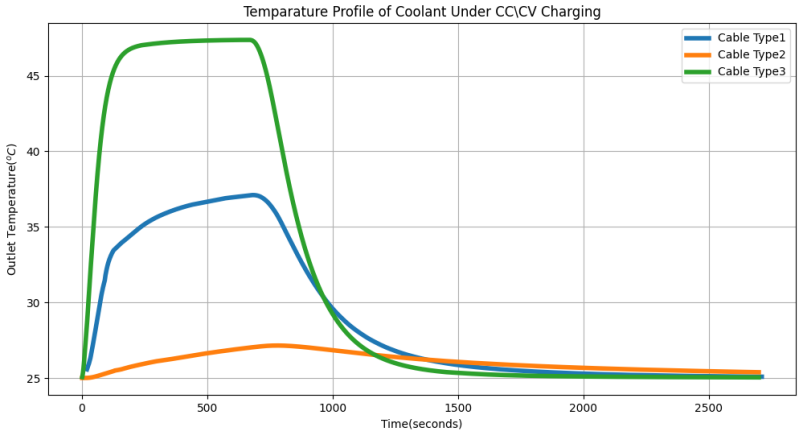

Figure 4.11: Coolant outlet temperature profile under CC-CV charging.

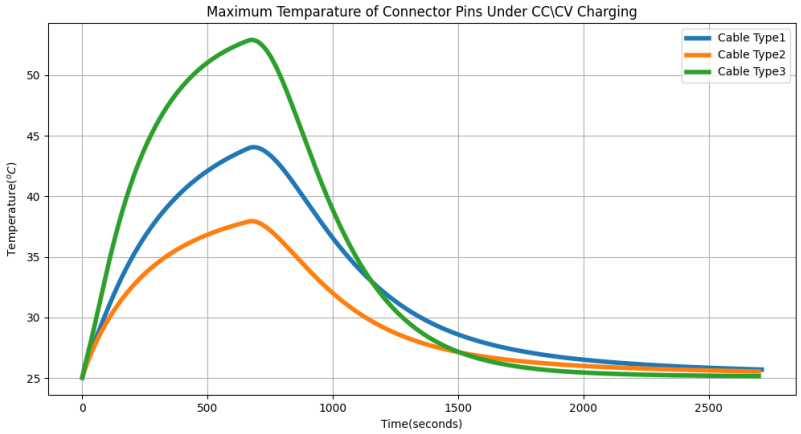

Figure 4.12: Maximum pin temperature under CC-CV charging.

Figures 4.11 and 4.12 present the coolant outlet temperature profile and the maximum pin temperature, respectively. The coolant outlet temperature is calculated as the mass flow average of the coolant cells at the outlet and is used to assess

the cooling demand. Cable Type 3 exhibits the highest coolant outlet temperature at 53°C, compared to 44°C for Type 1 and 37°C for Type 2. Given that the inlet temperature and mass flow rate are consistent across all cases, a higher outlet temperature indicates that more heat is absorbed by the coolant, signifying a more effective cooling system.
The heat generation rate in the DC pins is similar across the cables, so the differences in pin temperatures are primarily due to the varying coolant temperatures around the pins. As shown, Cable Type 3, which has the highest coolant temperature, also has the highest pin temperature. Conversely, Cable Type 2, with the lowest coolant temperature, exhibits the lowest pin temperature.

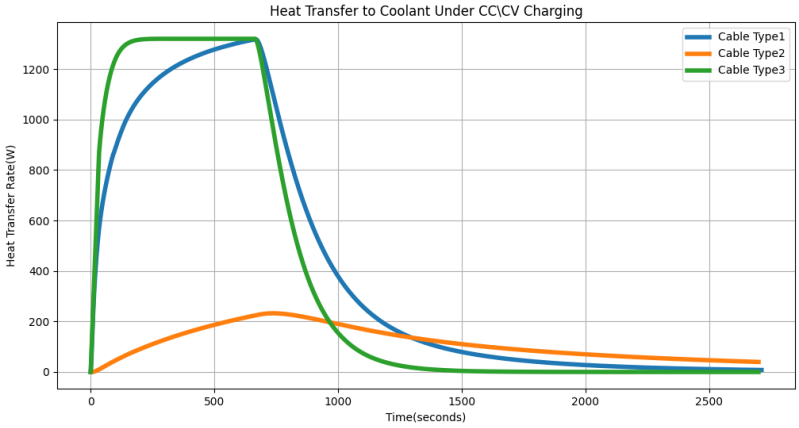

Figure 4.13: Heat transfer rate to coolant under CC-CV charging.

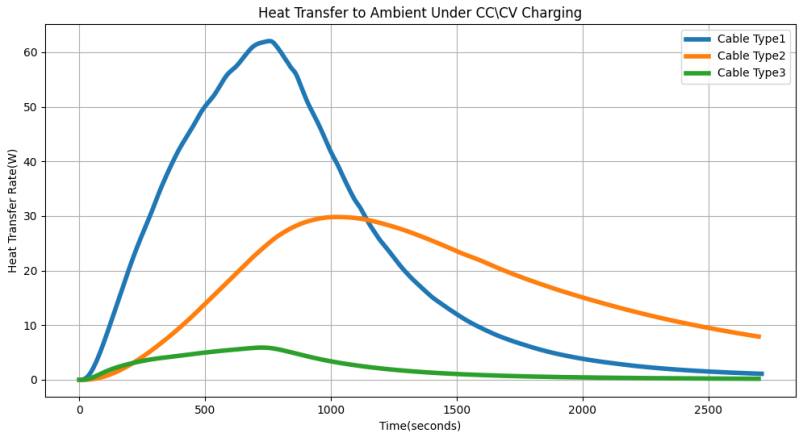

Figure 4.14: Heat transfer rate to ambient under CC-CV charging.

Figures 4.13 and 4.14 illustrate the heat transfer rates to the coolant and ambient air, respectively. Among the cables, Type 3 demonstrates the highest heat transfer to the coolant and the lowest heat transfer to the ambient, indicating that the coolant

is effectively removing most of the generated heat. This suggests that Cable Type 3 has the best cooling performance.
For Cable Type 1, the heat transfer to the coolant is similar to that of Type 3, but it increases with a delay. Additionally, the heat transfer to the ambient is higher in Type 1, suggesting that heat generation in this cable is higher, likely due to its smaller conductor cross-sectional area.
Cable Type 2 shows a much lower heat transfer rate to the coolant, and its heat transfer to the ambient is intermediate between the other two cables. This indicates that the cooling system in this cable is less efficient. However, the reduced heat generation in Cable Type 2, resulting from its larger conductor cross-sectional area, contributes to its relatively larger diameter and weight.

4.2 System simulation results

4.2.1 SOC and power module heat generation

This section presents the results of the SOC and power module heat generation calculations during the EV charging process. As illustrated in Figure 4.15, the EV battery is charged from 20% to 80% SOC over 45 minutes, and the charging curve aligns with the reference CC-CV charging pattern shown in Figure 3.10. The SOC increases more rapidly in the early stages of charging and gradually slows down due to the decrease in current. The results indicate that the total energy intake of the EV during the 45-minute charging period is 370 kWh.

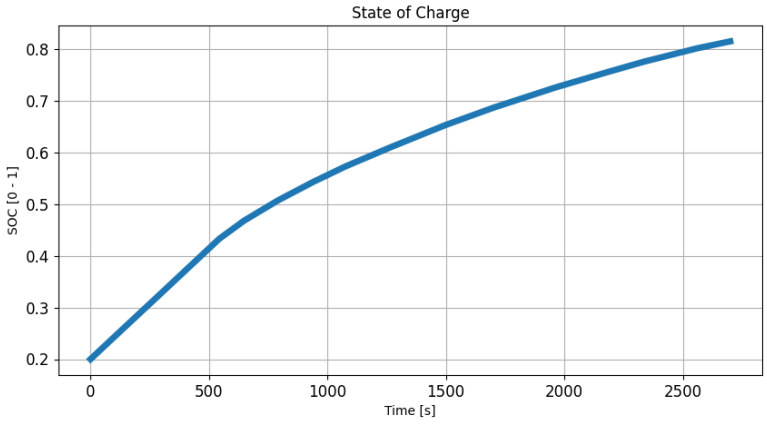

Figure 4.15: State of charge of the EV battery.

Figure 4.16 shows the heat generation rate of the power modules, calculated based on the power module efficiency curve shown in Figure 3.9. During the initial phase of charging, where the current remains constant, the voltage increases, leading to higher power consumption by the module and an improvement in its efficiency. This combination results in a slight rise in the heat generation rate. As the charging process continues and the current decreases, the power consumption of the module

also decreases, causing a gradual reduction in the heat generation rate. Over the entire charging process, the power module generates a total of 9.12 kWh of heat.

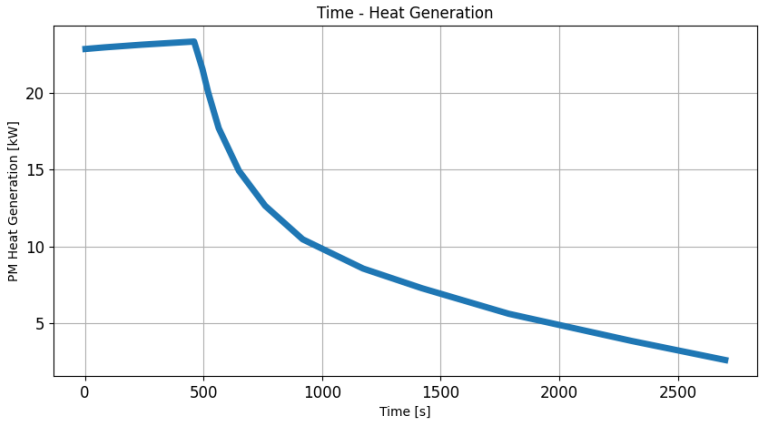

Figure 4.16: Power modules heat generation rate under CC-CV charging.

4.2.2 Cooling systems

This section presents the simulation results for the cooling systems applied to the power modules (Heatsink, Heatsink + PCM, Liquid Cooling, Immersion Cooling) and the liquid cooling system for the cables.

Figure 4.17 displays the power module temperature over time for the cooling systems. Among these, the **heatsink** cooling system results in the highest temperature, peaking at 58°C. The temperature increases as the EV power intake rises, and subsequently decreases gradually after the peak power is reached. Notably, there are two inflection points in the temperature curve—one at 35°C and the other at 53°C—corresponding to the activation of the three-speed fan controller. The fan speed increases at these temperatures, increasing the heat dissipation rate.
In the **heatsink + PCM** system, the temperature trend follows a similar pattern to the heatsink-only system until the PCM reaches its melting point. At this stage, the temperature stabilizes while the PCM absorbs heat during its phase change from solid to liquid. After the PCM is fully melted, the temperature increases slightly. Unlike the heatsink-only system, the temperature does not decrease as rapidly after the power intake peak, indicating the thermal buffering effect of the PCM.
The **liquid cooling** system records a maximum temperature of 50°C, which is 8°C lower than the maximum temperature observed in the heatsink-only system. After the power module reaches this threshold, the second speed of the dry air cooler is activated, leading to a higher heat dissipation rate compared to the previous two systems, eventually cooling the power module down to 34°C.
The **immersion cooling** system maintains the lowest temperature, peaking at just 35°C. This superior cooling performance is due to the coolant's high thermal capacity, which efficiently stores heat and acts as a large thermal reservoir, allowing the system to utilize a less powerful cooler, as the heat is dissipated gradually over time.

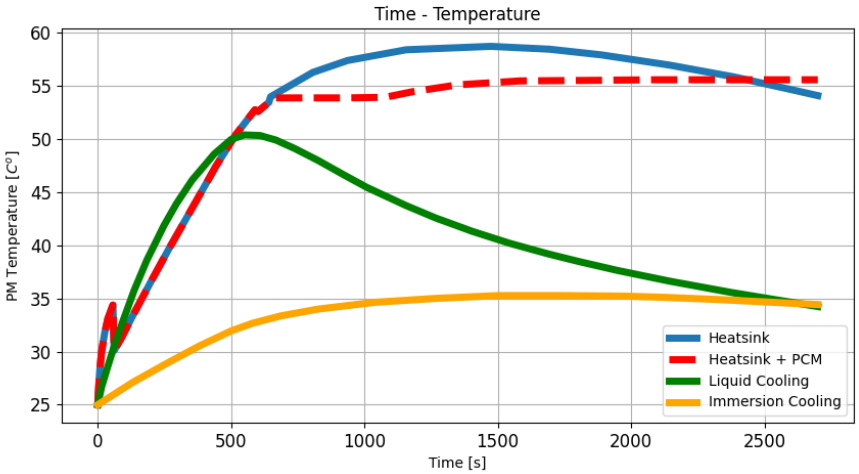

Figure 4.17: PM temperature over time in the immersiom cooling system.

Table 4.3 summarizes the total energy consumption of each cooling system during the charging process. The energy consumption values include the combined electricity usage of fans, pumps, and motors within each system. The results indicate that among the power module's cooling systems, the heatsink and heatsink + PCM consume the least energy, both at 130 Wh. Although adding PCM to the heatsink system helps maintain a lower temperature, it does not reduce overall energy consumption throughout the charging process. The liquid cooling system consumes the most energy at 340 Wh, followed by the immersion cooling system at 180 Wh. The lower energy consumption of the immersion cooling system is due to the coolant's ability to store heat effectively, thereby reducing the immediate cooling demand and allowing for the use of a less powerful cooler.

For the cable cooling system, since all three cables have the same coolant mass flow rate (1.8 liters per minute) and have close cooling demands, the same pump and cooler (OAC-100) are used across all cases. This results in a uniform energy consumption of 82 Wh for the cable cooling system, comprising 15 Wh for the pump and 67 Wh for the cooler.

	Energy Consumption
Heatsink	130 Wh
Heatsink + PCM	130 Wh
Liquid Cooling	340 Wh
Immersion Cooling	180 Wh
Liquid Cooling (For Cable)	82 Wh

Table 4.3: Cooling system's total energy consumption.

5
Conclusion

5.1 Thermal management of charging cable

Three different liquid-cooled cable structures are simulated, as shown in Table 5.1. The results indicate that Type 3, an oil-cooled cable with coolant cladding the copper, performed best in heat absorption. This design allows for the use of cables with a smaller copper cross-sectional area, enhancing flexibility. Type 1 also showed good heat dissipation but allowed some heat transfer to the surface, causing a temperature rise. However, it still reduced the conductor cross-sectional area, making the cable lighter and more flexible. Type 2 had the least heat absorption, necessitating more conductor material to meet temperature limits, resulting in higher mass and reduced flexibility.

Table 5.1: Summary of the final cable specifications.

Property	**Type 1**	**Type 2**	**Type 3**
Diameter (mm)	37.2	50	47
Copper Area (mm^2)	104 + 25	290 + 25	116 + 25
Coolant Flow (L/min)	1.8	1.8	1.8
Weight (kg/m)	2.1	4.3	2.7
Energy Loss (Wh)	370	128	330

5.2 Thermal management for power module

All cooling scenarios met the temperature limits for the power module. The heatsink scenario effectively managed temperatures, keeping the maximum below 60°C. Adding PCM to the heatsink helped maintain a more stable temperature, with a maximum of 55°C for an extended period. Liquid cooling showed excellent results, with the maximum temperature around 50°C and rapid cooling after peak temperatures, making it a reliable option. Immersion cooling kept temperatures well below the limit, suggesting it might be over-engineered for EV charging but suitable for continuous operation systems like data centers.

5.3 Energy loss in the whole system

Figure 5.1 summarizes the energy loss in the system. Considering the oil-cooled charging cable model and the liquid cooling system as the reference, the results demonstrate that charging a heavy-duty EV with a 1 MW MCS under a constant current-constant voltage (CC-CV) charging method for 45 minutes transfers 370 kWh of energy to the battery. The total system efficiency, including power modules and cables, is 97.3%. Of the input energy, 9.12 kWh (2.4%) is lost in the power modules, 0.41 kWh (0.1%) in the charging cable and its cooling system, and 0.34 kWh (0.1%) in the power module cooling system.

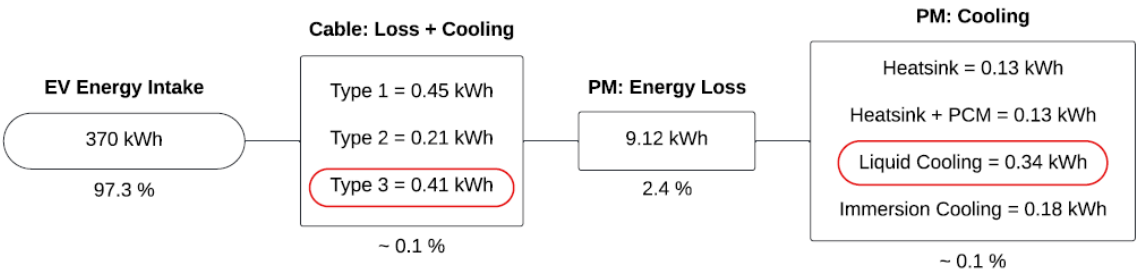

Figure 5.1: Summary of the final simulation results.

5.4 Future work

Building on the findings of this thesis, several avenues for future research are recommended to enhance the thermal management and overall efficiency of EV rapid charging systems.

Validation using experimental data

While this study has relied on simulations to assess the thermal management strategies, it is crucial to validate these models with experimental data. Conducting controlled laboratory experiments will provide empirical evidence to support the simulation results and ensure their accuracy in real-world applications. This step will also help in identifying any discrepancies and refining the models accordingly.

Assess models with different charging patterns

In this study, the simulations were conducted under two charging patterns: constant current-constant voltage, used as the reference charging pattern, and constant power, to assess an extreme scenario. However, different charging curves can significantly impact thermal management needs. Future research should explore a variety of charging profiles to understand their effects on the thermal behavior of batteries and charging equipment. This assessment will help in developing more robust thermal management systems that can adapt to diverse charging conditions.

Simulation of heat sources for power module

This study modeled the entire power modules as a lumped-element system, with heat generation calculated based on the efficiency curve provided by the manufacturer. To improve the precision of thermal management models, it is advantageous to simulate the main heat generation sources in power modules such as IGBTs and MOSFETs. Incorporating detailed simulations of these components will facilitate the design of more effective cooling systems. This approach will enhance the accuracy of thermal models and optimize cooling strategies.

Financial assessment

A financial analysis should be conducted to evaluate the cost-effectiveness of different thermal management solutions. This assessment should include initial investment costs, operational expenses, and potential savings from improved efficiency and reduced charging times. Understanding the financial implications will help in making informed decisions about the adoption and scaling of these technologies in commercial applications.

By addressing these aspects, future research can provide deeper insights and more practical solutions for the thermal management of fast charging systems, ultimately contributing to the advancement of electric vehicle infrastructure and technology.

Bibliography

[1] CharIN. Recommendations and requirements for mcs related standards bodies and solution suppliers. https://www.charin.global/news/charin-publishes-whitepaper-on-megawatt-charging-system-mcs/, November 2022. Version 1.0.

[2] Theodore L Bergman, Adrienne S Lavine, Frank P Incropera, and David P DeWitt. *Incropera's Principles of Heat and Mass Transfer*. Wiley Global Education, 2017.

[3] Yunus A. Çengel and Afshin J. Ghajar. *Heat and Mass Transfer: Fundamentals & Applications*. McGraw-Hill Education, New York, 6th edition, 2020.

[4] Henk Kaarle Versteeg and Weeratunge Malalasekera. *An Introduction to Computational Fluid Dynamics: The Finite Volume Method*. Pearson Education, 2007.

[5] Bengt Andersson, Ronnie Andersson, Love Håkansson, Mikael Mortensen, Rahman Sudiyo, and Berend van Wachem. *Computational Fluid Dynamics for Engineers*. Cambridge University Press, 2011.

[6] J. Walker. *Halliday and Resnick Fundamentals of Physics*. Wiley, United States, 2022.

[7] H. Liu. *Electrical Contacts: Principles and Applications*. CRC Press, United States, 2nd edition, 2017.

[8] Theodore Bohn. Debrief on the sae j3271 megawatt charging system standard for any large vehicle that rolls, flies or floats for the charin rmcs work group. https://www.anl.gov, May 2023. White Paper, Argonne National Laboratory.

[9] OMG EV Cable. Product catalog. https://www.omgevcable.com/cz/OMG%20ev%20cable.pdf, 2024. [Online Resource], Accessed: April 1, 2024.

[10] Henning Berg. *Batteries for Electric Vehicles: Materials and Electrochemistry*. Cambridge University Press, 2015.

[11] Jordi-Roger Riba and Pau Bas-Calopa. Analysing the pressure effect on the contact resistance of electrical connections. *European Journal of Physics*, 43(3):035806, mar 2022.

A

Appendix 1
HYC400 product datasheet

Figure A.1: HYC400 Product Datasheet, Page 1

Product data sheet

HYC400

100 kW to 400 kW DC-charging system for EVs

hypercharger by alpitronic

Technical Data

SYSTEM SPECIFICATION	
DC-connection standard	CCS2 up to 500 A (prepared for 600 A boost) (1) CHAdeMO up to 200 A CCS1 (2) GB/T (2)
Ambient	In- and outdoor installation
Working temperature	-30° to +55° C (3)
Humidity	5% - 95% relative humidity (non condensing)
Protection degree	IP54
IK-rating	IK10
Efficiency	97.5%
GRID	
Nominal voltage (rms)	380 V / 400 V / 480 V (4)
Max. input current (cont., rms)	600 A
Frequency	50 Hz / 60 Hz
Power factor with active PFC correction	>0,99
DC-OUTPUT	
Maximum DC output power (1)	100 kW (one Power-Stack), max. 300 A 200 kW (two Power-Stacks), max. 600 A 300 kW (three Power-Stacks), max. 600 A 400 kW (four Power-Stacks), max. 600 A
Granularity of output power	50 kW
Output DC voltage range	150 V - 1000 V
Maximum output current	Imax 500 A (prepared for 600 A boost) (1)
GENERAL	
DC-protocol standard	CCS1/2: SAE J1772 / EN 61851-23/DIN SPEC 70121; ISO 15118 CHAdeMO 1.2 GB/T 27930 (for automotive multicharger)
User registration	RFID reader (ISO/IEC 14443A/B, ISO/IEC 15693) Credit Card reader with QR-Code-reader (optional)
Network Connection	LTE/UMTS/GSM Modem 4G/3G/2G 10/100Base-T Ethernet
Charging infrastructure communication protocol	Open Charge Point Protocol (OCPP) 1.6 J, ready for 2.0 J
User Interface	15,6" screen, 4 buttons
MECHANICAL	
Dimensions (HxWxL)	2235 x 732 x 663 mm
Weight	375 kg up to 775 kg (1)

(1) Preliminary data to be verified (2) Only upon special request by OEMs (3) Derating tbd (4) 480 V only upon special request

Via di Mezzo ai Piani, 33
39100 Bolzano BZ, Italy
info@hypercharger.it
www.hypercharger.it
Tel.: +39 0471 1961 000

Figure A.2: HYC400 Product Datasheet, Page 2

B

Appendix 2
Cooling system components

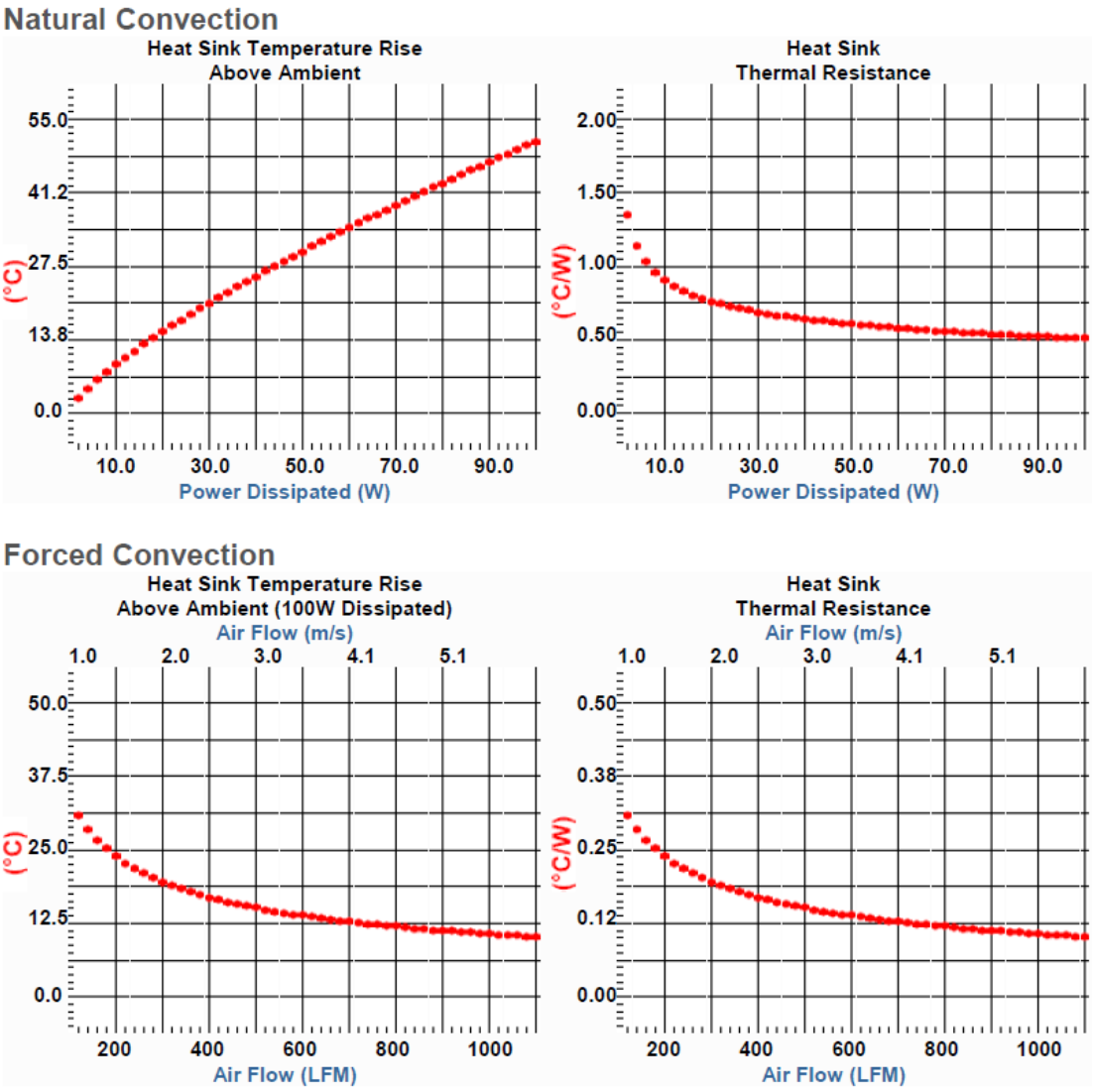

Figure B.1: Thermal performance data for Heatsink 62335 by AAVID Thermalloy.

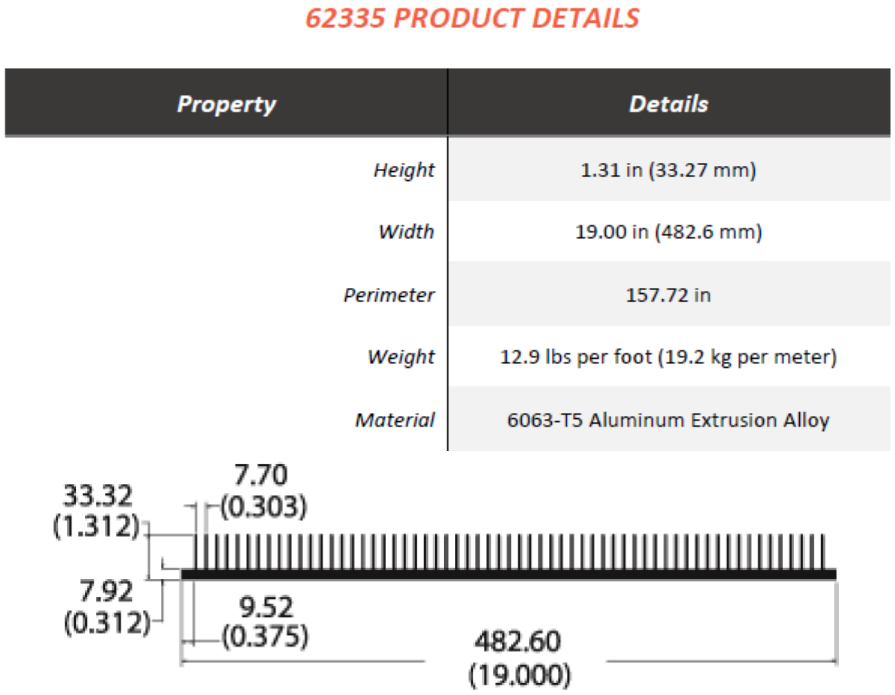

62335 PRODUCT DETAILS

Property	Details
Height	1.31 in (33.27 mm)
Width	19.00 in (482.6 mm)
Perimeter	157.72 in
Weight	12.9 lbs per foot (19.2 kg per meter)
Material	6063-T5 Aluminum Extrusion Alloy

Figure B.2: Dimensional and material specifications of Heatsink 62335 by AAVID Thermalloy.

Technical parameter

Dimension (mm)	Model	Voltage (VAC)	Frequency (Hz)	Current (AMP)	Power (Watts)	Speed (RPM)	Air Flow (CFM)/m³/min	Pressure (mmH₂O)	Noise (dBA)	Weight (Gram)
150X150X51	PD150B-110	110/120	50/60	0.38	24	2600	180/5.0	0.38	49.6	960
	PD150B-127	110/127	50/60	0.35	25	2600	180/5.0	0.38	49.6	960
	PD150B-220	220/240	50/60	0.18	28	2600	180/5.0	0.38	49.6	960

Outline drawing

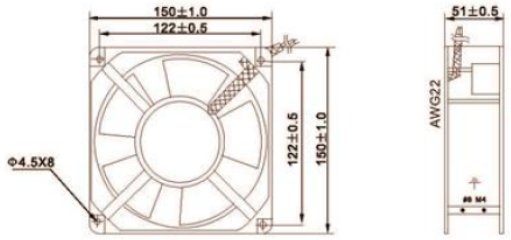

Figure B.3: Technical specifications of PD150B-220 fan by Salzer.

Property	Details
Plate Details	Extruded Aluminum
Tube Material	Copper 9.5mm O.D. x 1.24mm wall
Standard Finish	Unfinished
Epoxy	Aluminum Filled - High Thermal Conductivity

Measurement	mm	in
Width	177.8	7
Thickness	15.24	0.55

PERFORMANCE – 6 PASS

Figure 2

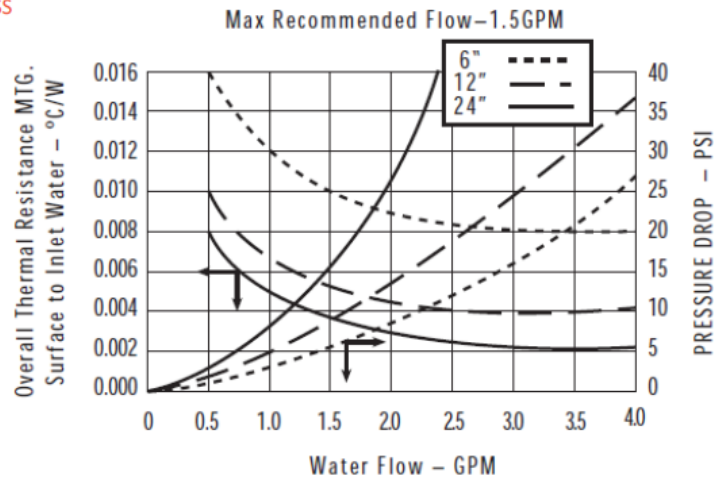

Figure B.4: BOYD 6-Pass Cold Plate, technical data.

Technical data

12V and 24V fan drive

Type of cooler [3]	Voltage [V]	Drive [kW]	Speed [rpm]	Amperage [A]	Protection class	Fan Ø [mm]	Perm. pressure [bar] Static	Perm. pressure [bar] Dynamic	Max. volume flow [l/min]	Weight [kg]
OAC100-01	12	0.09	3950	7.2	IP68	190			50	6
OAC100-02	24	0.06	3625	2.6	IP68	190				6
OAC200-01	12	0.10	2838	8.2	IP68	280			100	11
OAC200-02	24	0.11	2925	4.4	IP68	280				11
OAC250-01	12	0.10	2838	8.2	IP68	280				13
OAC250-02	24	0.11	2925	4.4	IP68	280			120	13
OAC300-01	12	0.22	3080	18.4	IP68	350				16
OAC300-02	24	0.23	2730	9.4	IP68	350				16
OAC400-01	12	0.22	3080	18.4	IP68	350	26	14		22
OAC400-02	24	0.23	2730	9.4	IP68	350			200	22
OAC500-01	12	0.24	2600	20.2	IP68	385				30
OAC500-02	24	0.24	2700	9.8	IP68	385				30
OAC600-01	12	2 x 0.10	2838	2x8.2	IP68	280			250	43
OAC600-02	24	2 x 0.11	2925	2x4.4	IP68	280				43
OAC700-01	12	2 x 0.24	2600	2x20.2	IP68	385				53
OAC700-02	24	2 x 0.24	2700	2x9.8	IP68	385			350	53
OAC800-01	12	2 x 0.24	2600	2x20.2	IP68	385				81
OAC800-02	24	2 x 0.24	2700	2x9.8	IP68	385				81

[3] Max. medium temperature: 110 °C (higher temperatures on request) / Max. ambient temperature: 60 °C
Other motors on request

Performance diagramme

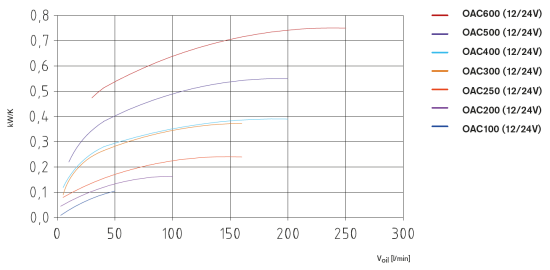

Diagramme of pressure loss

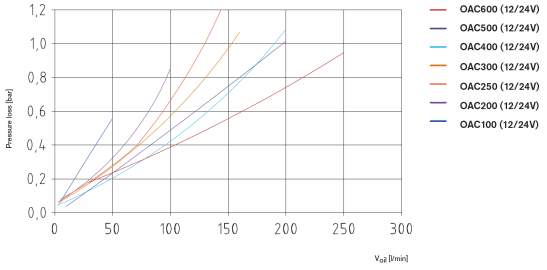

Figure B.5: KTR, OAC-400 cooler, technical data.

230/400V with 50 Hz; 460V with 60 Hz fan drive														
Type of cooler [2]	Driving power [kW]		Speed [rpm]		Amperage [A]		Protection class		Fan Ø [mm]	Noise [1] [dbA]	Perm. pressure [bar]		Max. volume flow [l/min]	Weight [kg]
	50 Hz	60 Hz	50 Hz	60 Hz	50 Hz	60 Hz	Standard	Marine			Static	Dynamic		
OAC100-03 C	0.07	0.08	2500	2700	0.29	0.33	IP54	–	200	64			50	16
OAC200-03 C	0.12	0.16	2450	2650	0.55	0.72	IP54	–	250	69			100	16
OAC200-03	0.18	0.21	1350	1650	0.58	0.57	IP55	IP56	280	66			100	16
OAC250-03	0.18	0.21	1350	1650	0.58	0.57	IP55	IP56	280	66			120	20
OAC300-03-4	0.37	0.43	1370	1670	1.04	1.02	IP55	IP56	380	76			160	24
OAC300-03-6	0.18	0.21	850	1020	0.87	0.88	IP55	IP56	380	63			160	24
OAC300-03 D	0.14	0.17	1400	1600	0.35	0.32	IP44	-	350	72			160	21
OAC400-03-4	0.37	0.43	1370	1670	1.04	1.02	IP55	IP56	380	76	26	14	200	29
OAC400-03-6	0.18	0.21	850	1020	0.87	0.88	IP55	IP56	380	63			200	29
OAC400-03 D	0.14	0.17	1400	1600	0.35	0.32	IP44	-	350	72			200	26
OAC500-03-4	0.37	0.43	1370	1670	1.04	1.02	IP55	IP56	380	78			200	37
OAC500-03-6	0.18	0.21	850	1020	0.87	0.88	IP55	IP56	380	63			200	37
OAC600-03	0.75	0.86	1440	1740	1.79	1.72	IP55	IP56	520	78			250	57
OAC700-03	0.75	0.86	1440	1740	1.79	1.72	IP55	IP56	520	78			350	70
OAC800-03	1.5	1.75	1435	1730	3.3	3.3	IP55	IP56	630	78			350	97
OAC850-03	2.2	2.55	965	1165	5.2	4.75	IP55	IP56	750	79			350	130
OAC900-03-6	2.2	-	965	-	5.2	-	IP55	IP56	900	85			450	173
OAC900-03-4	7.5	-	1465	-	14.3	-	IP55	IP56	900	97			450	205
OAC1000-03-8	1.5	-	700	-	4.65	-	IP55	IP56	900	81			530	154
OAC1000-03-6	2.2	-	965	-	5.2	-	IP55	IP56	900	87	21	14	530	187
OAC1000-03-4	7.5	-	1465	-	14.3	-	IP55	IP56	900	97			530	212
OAC2000-03-8	4	-	720	-	10.9	-	IP55	IP56	1000	86			700	329
OAC2000-03-6	7.5	-	980	-	16	-	IP55	IP56	1000	92			700	357
OAC2000-03-4	18.5	-	1470	-	35	-	IP55	IP56	1000	100			700	429

[1] Measurement based on 50 Hz operation
[2] Max. medium temperature: 110 °C (higher temperatures on request)/Max. ambient temperature: 40 °C

Performance diagramme

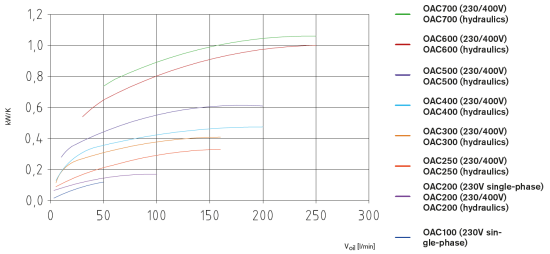

Diagramme of pressure loss

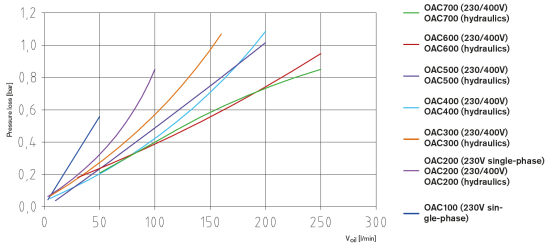

Figure B.6: KTR, OAC-100 cooler, technical data.

Properties	3M™ Fluorinert™ Electronic Liquid FC-3283
Appearance	Clear, colorless
Average Molecular Weight	521
Boiling Point (@ 1 atm)	128°C (262.4°F)
Pour Point	-65°C (-85°F)*
Calculated Critical Temperature	235 (°C)
Calculated Critical Pressure	1.22 x 10^6 (pa)
Vapor Pressure	1.44 x 10^3 (pa)
Latent Heat of Vaporization (at normal boiling point)	78 (J/g)
Liquid Density	1820 (kg/m^3)
Kinematic Viscosity	0.75 (cSt)
Absolute Viscosity	1.4 (cP)
Liquid Specific Heat	1100 J kg^{-1} $°C^{-1}$
Liquid Thermal Conductivity	0.066 W m^{-1} $°C^{-1}$
Coefficient of Expansion	0.0014 $°C^{-1}$
Surface Tension	14.6 (dynes/cm)
Refractive Index	1.28
Water Solubility	7 (ppmw)
Ozone Depletion Potential	0
Flash Point	None

*Temperatures between the freeze point and melt point are considered super cooled. Talk to a Tech Service Engineer for more information.

Properties	3M™ Fluorinert™ Electronic Liquid FC-3283
Dielectric Strength (0.1" gap)	>40 (kV)
Dielectric Constant (@ 1 kHz)	1.9
Electrical Resistivity (ASTM D-257)	1 x 10^{15} (ohm cm)

Figure B.7: 3M FC-3283 Dielectric Coolant Technical Data - Page 1.

Specific Heat (J kg^{-1} $°C^{-1}$) = 1014 + 1.554 (T, °C)
Thermal Conductivity (W m^{-1} $°C^{-1}$) = 0.065 – 0.000056 (T, °C)
Density (kg/m^3) = 1878 – 2.455 (T, °C)
Log_{10} (Vapor Pressure (pascals)) = 10.237 – (2110/(T, K))

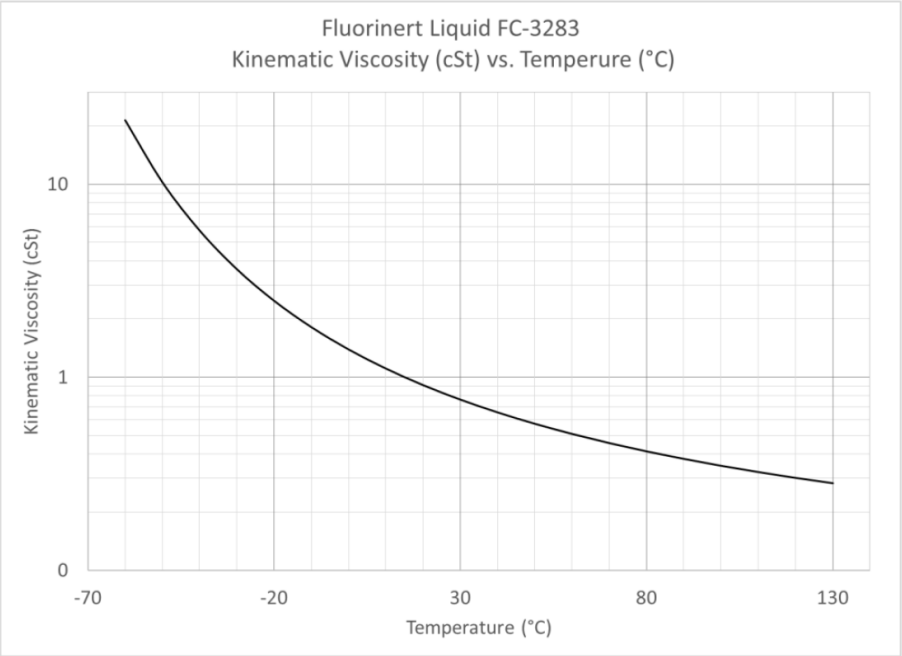

Figure B.8: 3M FC-3283 Dielectric Coolant Technical Data - Page 2.

C

Appendix 3
CFD results

- Cable Type One:

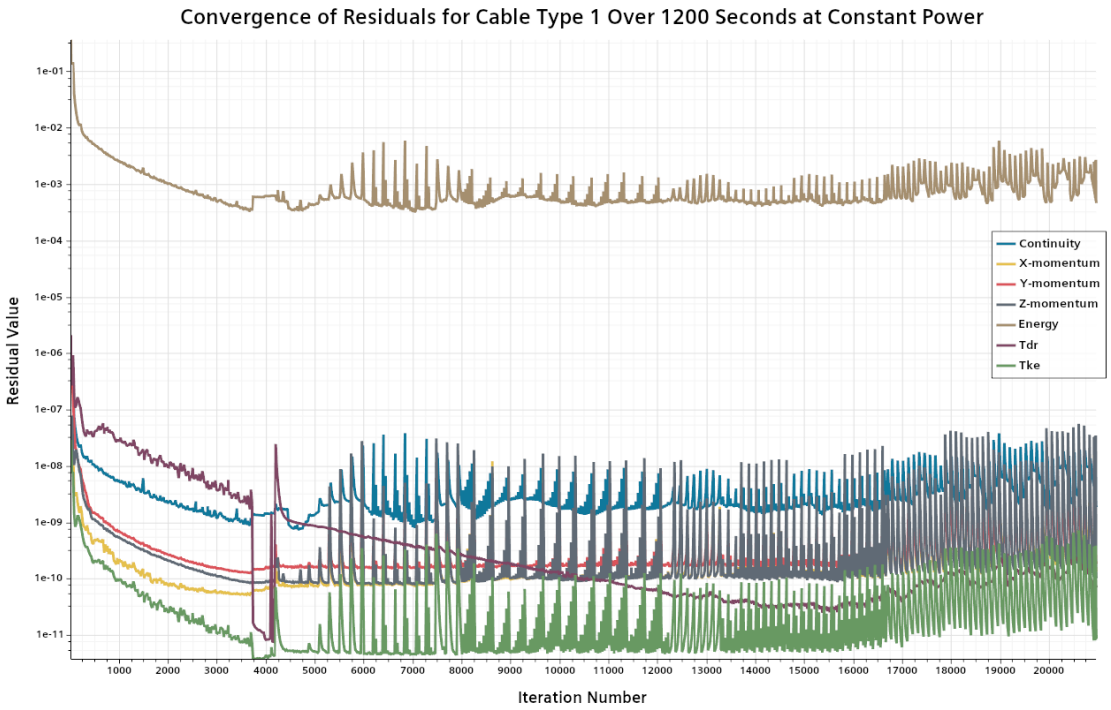

Figure C.1: Residual convergence for cable Type 1 under constant power.

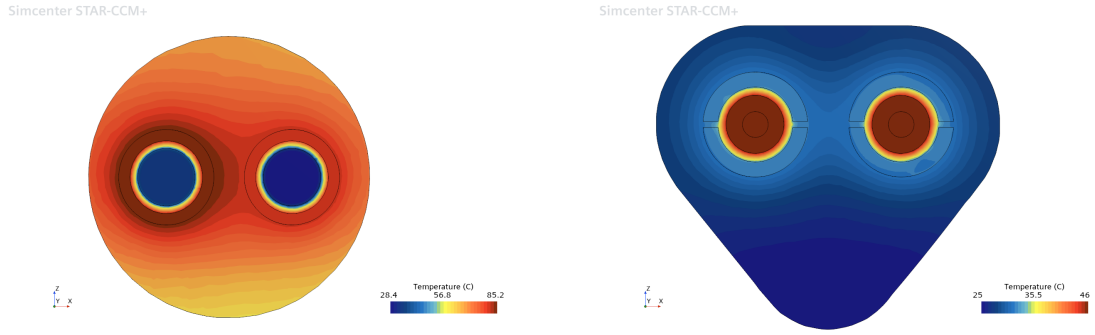

Figure C.2: Temperature contours for Cable Type 1 after 20 minutes of constant power: (a) cable cross-section, (b) plug cross-section.

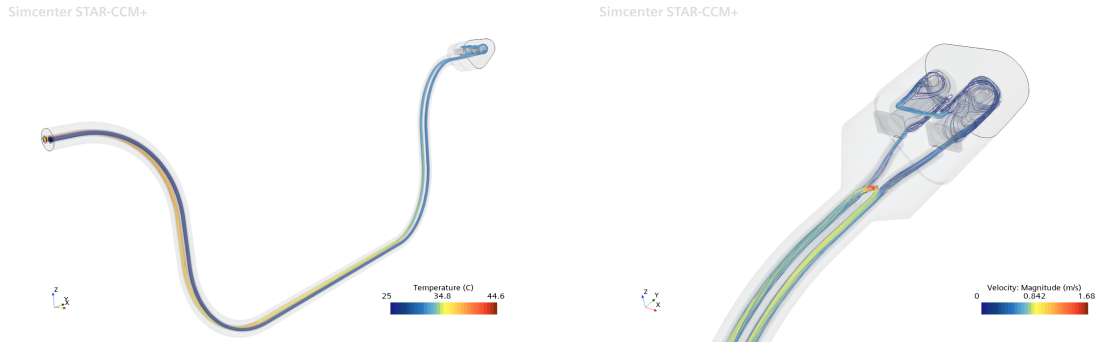

Figure C.3: Coolant temperature for Cable Type 1 after 20 minutes of constant power: (a) full cable view, (b) connector loop.

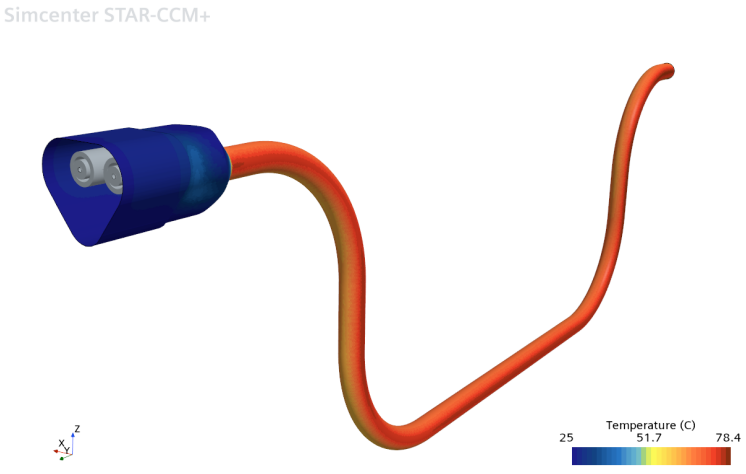

Figure C.4: Surface temperature of Cable Type 1 after 20 minutes of constant power.

- Cable Type Two:

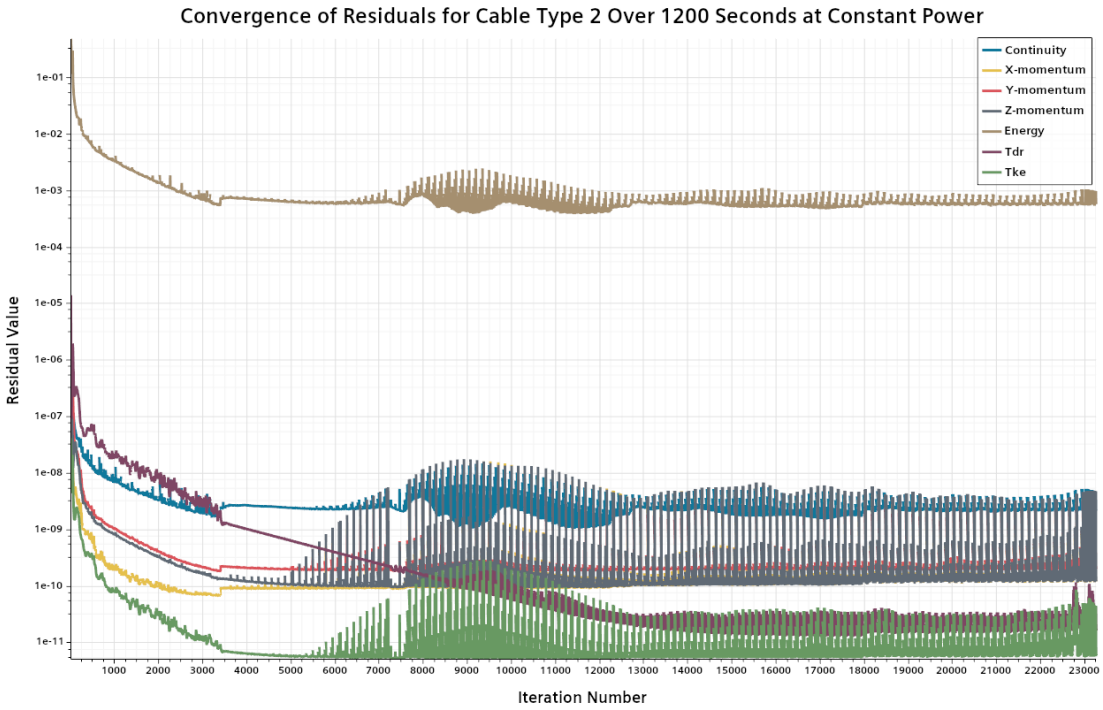

Figure C.5: Residual convergence for cable Type 2 under constant power.

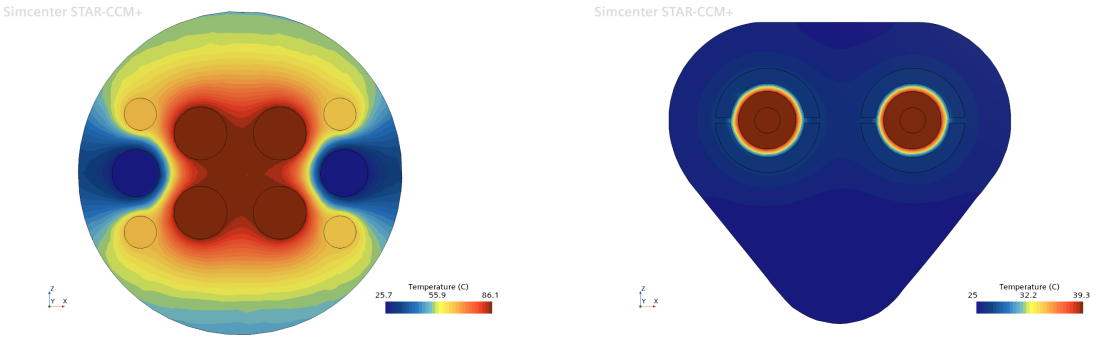

Figure C.6: Temperature contours for Cable Type 2 after 20 minutes of constant power: (a) cable cross-section, (b) plug cross-section.

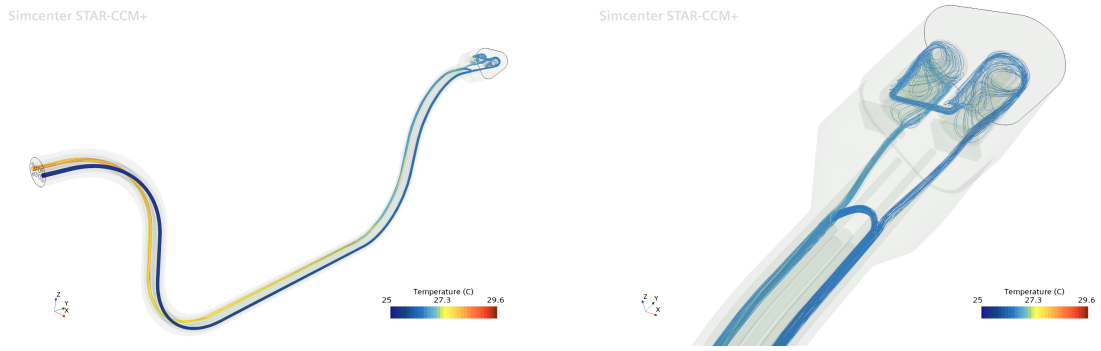

Figure C.7: Coolant temperature for Cable Type 2 after 20 minutes of constant power: (a) full cable view, (b) connector loop.

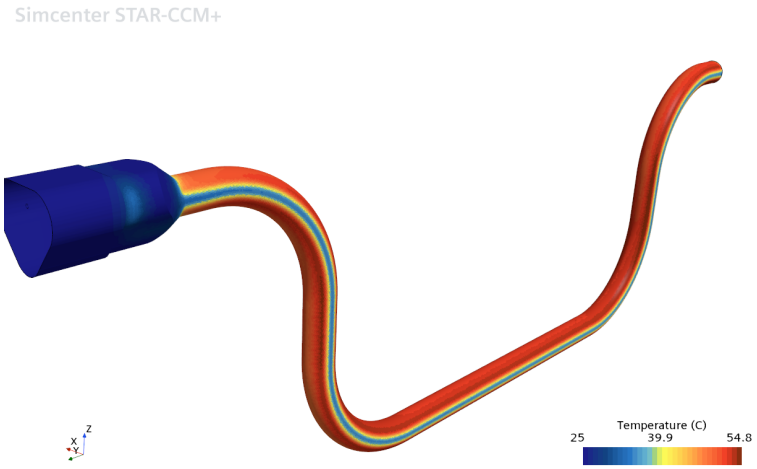

Figure C.8: Surface temperature of Cable Type 2 after 20 minutes of constant power.

- Cable Type Three:

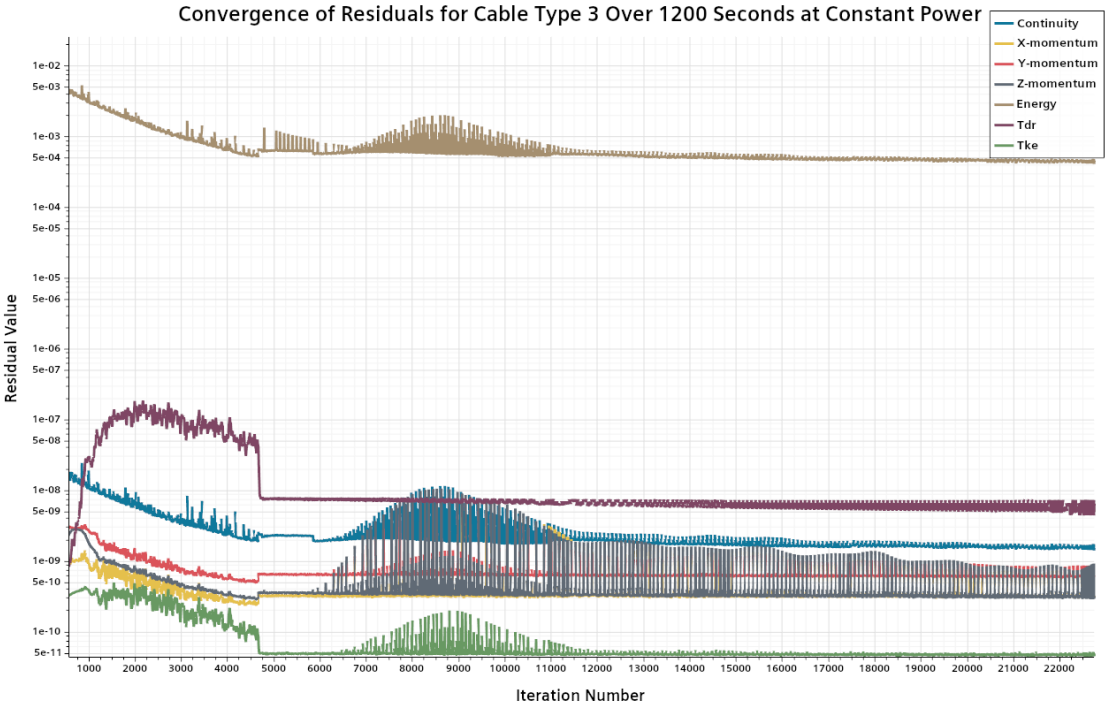

Figure C.9: Residual convergence for cable Type 3 under constant power.

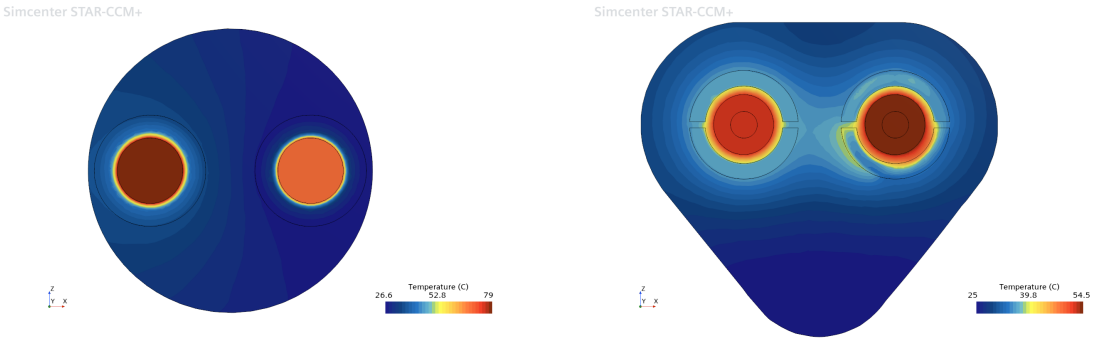

Figure C.10: Temperature contours for Cable Type 3 after 20 minutes of constant power: (a) cable cross-section, (b) plug cross-section.

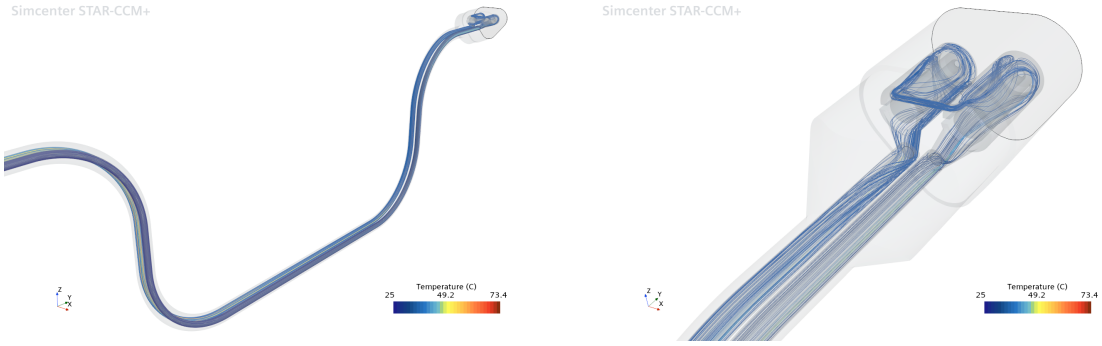

Figure C.11: Coolant temperature for Cable Type 3 after 20 minutes of constant power: (a) full cable view, (b) connector loop.

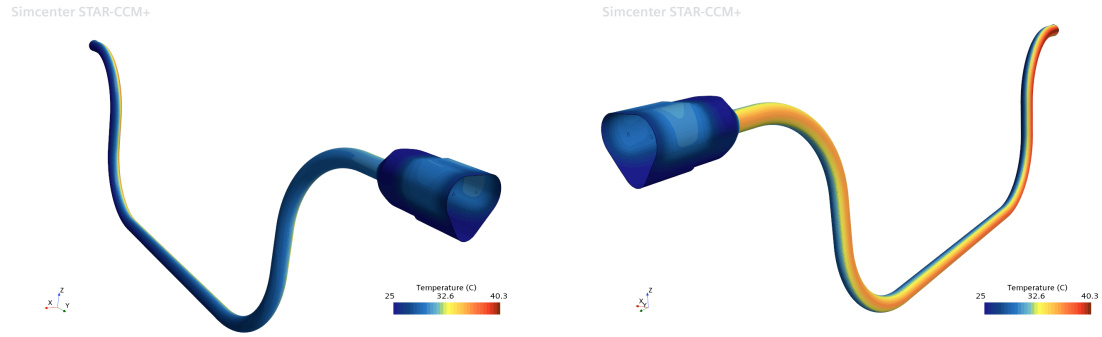

Figure C.12: Surface temperature of Cable Type 3 after 20 minutes of constant power: (a) Inlet side, (b) Return side.

DEPARTMENT OF SOME SUBJECT OR TECHNOLOGY
CHALMERS UNIVERSITY OF TECHNOLOGY
Gothenburg, Sweden
www.chalmers.se

CHALMERS
UNIVERSITY OF TECHNOLOGY